3D Bioprinting of Multifunctional Dynamic Nanocomposite Bioinks Incorporating Cu-Doped Mesoporous Bioactive Glass Nanoparticles for Bone Tissue Engineering

Hui Zhu, Mahshid Monavari, Kai Zheng, Thomas Distler, Liliang Ouyang, Susanne Heid, Zhaorui Jin, Jiankang He, Dichen Li, and Aldo R. Boccaccini*

Bioprinting has seen significant progress in recent years for the fabrication of bionic tissues with high complexity. However, it remains challenging to develop cell-laden bioinks exhibiting superior physiochemical properties and bio-functionality. In this study, a multifunctional nanocomposite bioink is developed based on amine-functionalized copper (Cu)-doped mesoporous bioactive glass nanoparticles (ACuMBGNs) and a hydrogel formulation relying on dynamic covalent chemistry composed of alginate dialdehyde (oxidized alginate) and gelatin, with favorable rheological properties, improved shape fidelity, and structural stability for extrusion-based bioprinting. The reversible dynamic microenvironment in combination with the impact of cell-adhesive ligands introduced by aminated particles enables the rapid spreading (within 3 days) and high survival (>90%) of embedded human osteosarcoma cells and immortalized mouse bone marrow-derived stroma cells. Osteogenic differentiation of primary mouse bone marrow stromal stem cells (BMSCs) and angiogenesis are promoted in the bioprinted alginate dialdehyde-gelatin (ADA-GEL or AG)-ACuMBGN scaffolds without additional growth factors in vitro, which is likely due to ion stimulation from the incorporated nanoparticles and possibly due to cell mechanosensing in the dynamic matrix. In conclusion, it is envisioned that these nanocomposite bioinks can serve as promising platforms for bioprinting complex 3D matrix environments providing superior physiochemical and biological performance for bone tissue engineering.

H. Zhu, J. He, D. Li
State Key Laboratory for Manufacturing Systems Engineering
Xi'an Jiaotong University
Xi'an 710054, P. R. China
H. Zhu, M. Monavari, K. Zheng, T. Distler, S. Heid, Z. Jin, A. R. Boccaccini
Department of Materials Science and Engineering
Institute of Biomaterials
Friedrich-Alexander-University Erlangen-Nuremberg
91058 Erlangen, Germany
E-mail: aldo.boccaccini@ww.uni-erlangen.de
L. Ouyang
Department of Mechanical Engineering
Biomanufacturing and Rapid Forming Technology Key Laboratory
of Beijing, "Biomanufacturing and Engineering Living Systems"
Innovation International Talents Base (111 Base)
Tsinghua University
Beijing 100084, P. R. China

1. Introduction

Bone regeneration approaches have been developed for decades to treat bone defects, fractures, or tumor resections by combining bone substitute materials that resemble the natural extracellular matrix (ECM) of bone. For successful bone regeneration, bone substitutes are required to be 3D porous structures with sufficient mechanical strength, suitable degradation rate, biocompatibility, bioactivity, and biological functions such as osteogenesis and angiogenesis. 3D bioprinting has emerged as a promising technique to generate tissue-like constructs using cell-laden hydrogels, which are known as bioinks, by layer-by-layer fabrication methods.[1] 3D bioprinting has shown potential to recreate complex tissues by distributing cell and biomaterial precisely in 3D,[1,2] using different methods such as micro-extrusion,[3] material jetting,[4] and vat polymerization methods.[5] Among those technologies, extrusion-based printing is one of the most selected methods for printing cells because it combines simplicity, affordability, and versatility to fabricate large-scale 3D constructs with a high cell density.[6] One challenge in extrusion-based bioprinting remains the lack of bioinks capable of meeting the demands of exhibiting specific rheological properties before printing, supporting high cell viability, as well as keeping scaffold shape and mechanical properties after printing.[7] Specifically for bone regeneration applications, bioinks should stimulate osteogenic differentiation, encourage angiogenesis and vascular network infiltration, and induce ECM mineralization in vitro.[8,9]

Among the numerous efforts made to obtain the desired performance of hydrogel-based bioinks, organic/inorganic composite ink formulations in which inorganic fillers are mixed with hydrogels represent an attractive approach to achieve the conflicting requirements of a cell-friendly microenvironment and adapted mechanical properties of scaffolds.[10–12] Typically, inorganic particles such as hydroxyapatite,[13] α-, β-tricalcium phosphate (TCP),[14] bioactive glass, nanoclays,[15] nanosilicates,[16] and graphene oxide[17] are added to biocompatible hydrogels to manipulate rheological properties of the bioinks (e.g., shear-thinning behavior and yield strength) in order to improve the printability of inks and shape fidelity of

printed constructs. However, conventional physical combination of inorganic fillers and hydrogels may lead to a disruption of the crosslinked polymer network and to inhomogenous distribution of particles. To address this issue, approaches based on increased affinity between rigid nanostructured surfaces and polymers must be considered to fabricate bioinks with superior mechanical properties. Very recently, Zandi et al.[18] presented a printable composite hydrogel exploiting the interactions between negatively charged glycosaminoglycan nanoparticles and positively charged nanoclay edges. In another study, Lee et al. reported that sub-100 nm silica nanoparticles (NPs) functionalized with cationic surface could crosslink anionic polysaccharides effectively due to electrostatic interaction, thus enhancing the printing fidelity of the fabricated structure significantly.[19] Nevertheless, it remains a pressing and significant challenge to design smart bioinks, not only to improve the mechanical performance of the printed structure but also to realize their biological functionalities for cell fate guidance, as well as to capture the native dynamics of the natural ECM to reproduce the physicochemical microenvironment of bone tissue.[20–23] Natural bone is highly vascularized, thus the osteogenesis–angiogenesis coupling process is pivotal in designing strategies for bone repair.[24] Previous work has shown the possibility of incorporating bioactive glass nanoparticles (BGNPs) into hydrogels for promoting the mineralization of the resulting constructs,[25] and for inducing early osteogenesis/chondrogenic differentiation.[26] Besides, copper-doped mesoporous BGNPs (CuMBGNs) are well-known for their ability to promote pro-angiogenic and osteo/odontogenic functions in bone and wound healing.[27,28] On the other hand, alginate dialdehyde-gelatin (ADA-GEL or AG) hydrogels have been proven to be cytocompatible offering a versatile biomaterial for cell encapsulation and for 3D

bioprinting.[25,26,29,30] Therefore, an advanced nanocomposite bioink is expected to be developed here, introducing aminated CuMBGNs (ACuMBGNs) with free amino groups ($-NH_2$) to act as nanocrosslinkers inside the AG system with free aldehyde groups. Associated multiple functions are expected to be realized through this approach, which are presented in this study.

Thus, we report here the formation of advanced AG-based bioinks based on dynamic covalent chemistry that incorporate aminated mesoporous bioactive glass nanoparticles (AMBGNs) or ACuMBGNs as a versatile strategy to generate cell-laden bioprinted constructs with enhanced bioactivity, shape fidelity, adjustable degradation, self-healing property, cell compatibility as well osteogenic differentiation and angiogenic effects, as shown in **Figure 1**. The double crosslinking reversible imine bonds linking aldehyde moieties of alginate dialdehyde and amino moieties on both functionalized particles and gelatin are hypothesized to confer the system superior mechanical performance and self-assembling abilities. Furthermore, by adopting transglutaminase (mTG) as another reagent for the post-crosslinking of the printed constructs, a desirable degradation behavior can be obtained. These multifunctional bioinks with potential osteogenic and angiogenic-inducing capacities are attractive for developing cell-laden complex constructs for bone tissue engineering.

2. Results

2.1. Preparation and Characterization of Nanoparticles

Figure 2A illustrates the formation and surface functionalization mechanisms of MBGNs. Cetrimonium bromide (CTAB)
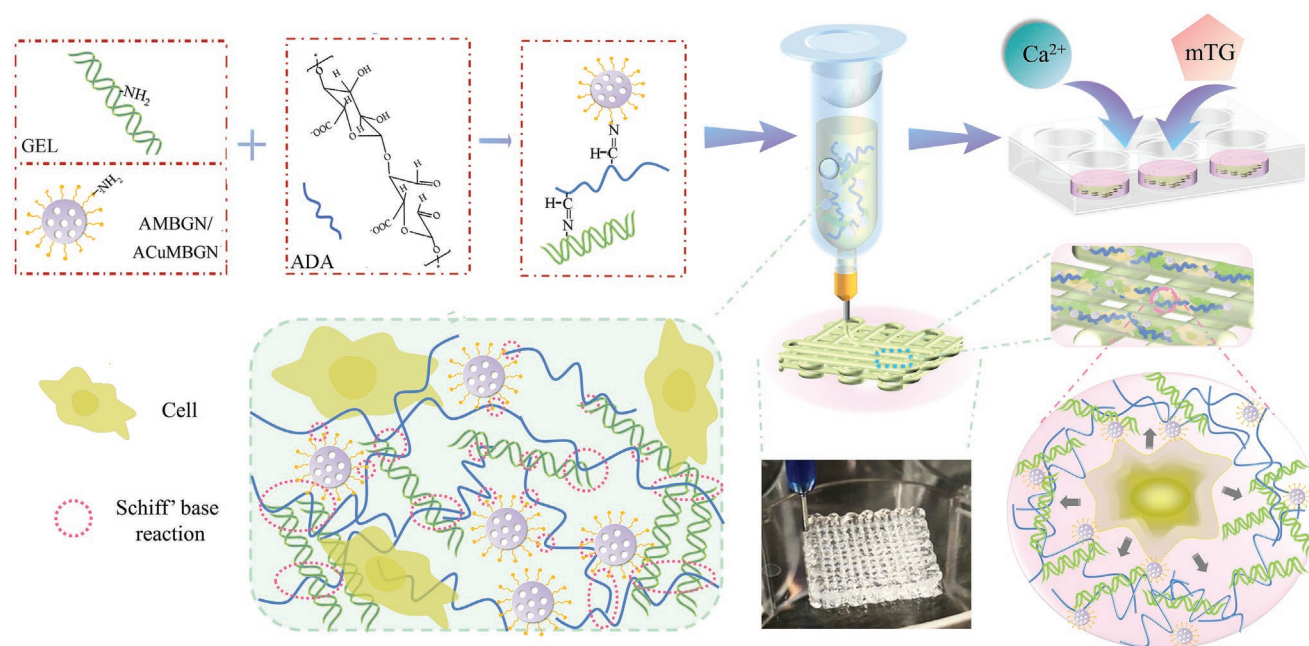
Figure 1. Schematic representation of the nanocomposite bioinks based on Schiff' base reaction of aminated MBGNs (AMBGNs) or ACuMBGNs, gelatin (GEL) and alginate dialdehyde (ADA), and the bioprinting process.
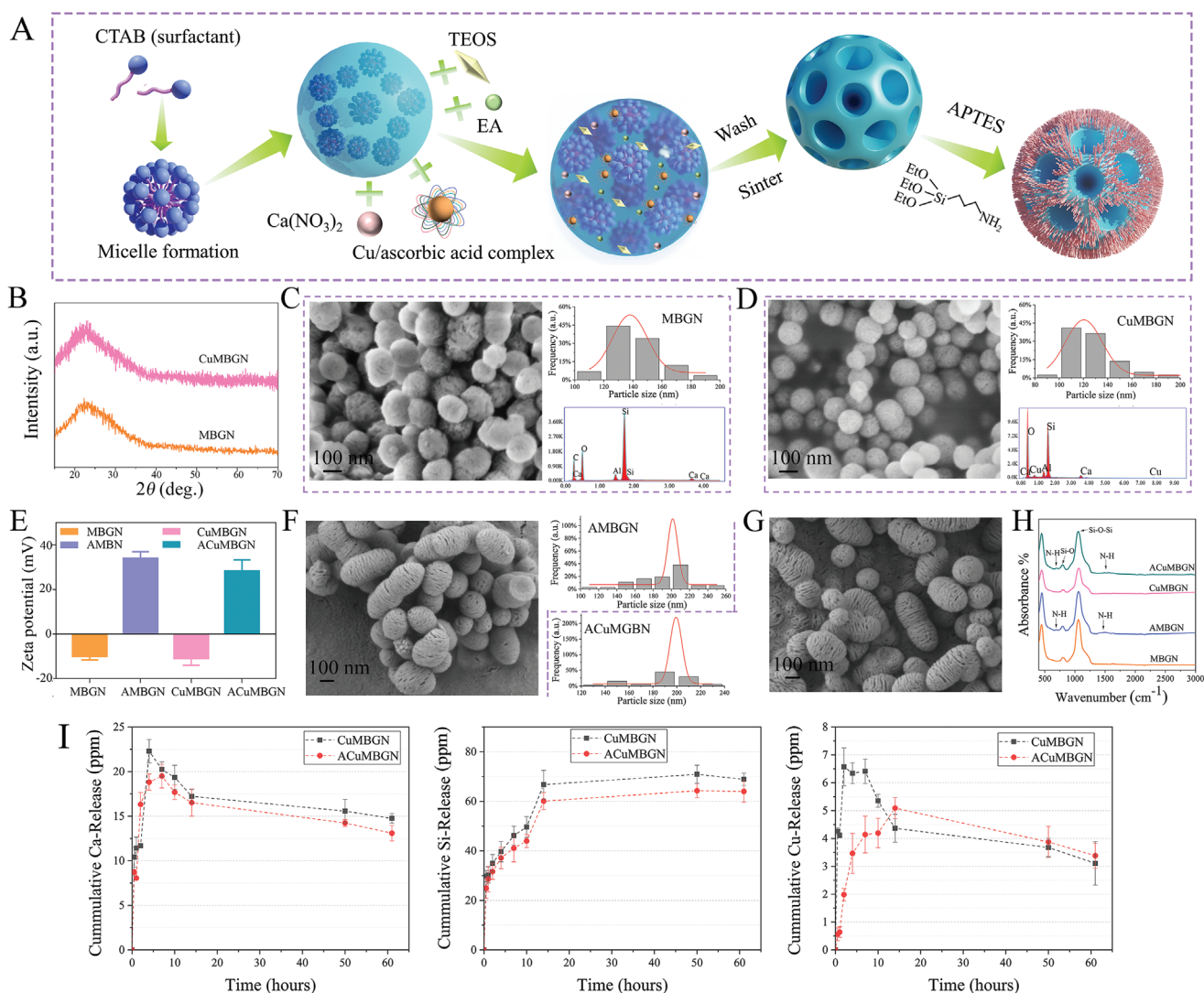
Figure 2. A) Schematic diagram of the formation and surface functionalization mechanisms of MBGNs. B) Amorphous structure of the synthesized Cu-doped and Cu-free MBGNs confirmed by XRD. SEM images, particle size, and element analysis of C) MBGNs and D) CuMBGNs. E) Zeta potential of MBGNs and CuMBGNs before and after surface amination. SEM images and particle size analysis results of F) AMBGNs and G) ACuMBGNs. H) FTIR spectra of MBGNs and AMBGNs before and after surface amination. I) Calcium, silicon, and copper ions release from CuMBGNs and ACuMBGNs during 3 days' immersion in Tris-buffer solutions at 37 °C.

micelle can self-assemble with ethyl acetate (EA) to form spherical vesicles during the sol–gel process, which works as template. Then the bioactive glass (BG) sol is hydrolyzed by ammonia molecules catalyzing and it condenses at the template surface by hydrogen bondings.[31,32] After washing and calcination, CTAB can be removed to obtain the mesoporous BGNPs. With regard to the chemical modification of MBGNs by amino groups, 3-aminopropyl triethoxy silane (APTES) was allowed to react with the glass surface in toluene under constant stirring while refluxing. The surface hydroxyl groups of MBGNs (silanol groups) are condensing with the ethoxy groups of APTES, and this process can be accelerated by the elevated temperature used.[33] The X-ray diffraction analysis (XRD) patterns of MBGNs and CuMBGNs after calcination at 700 °C are shown in Figure 2B, confirming the amorphous nature of the glass nanoparticles. The addition of Cu/ascorbic

acid complex does not introduce any structural change in the particles. The synthesized MBGNs and CuMBGNs show uniform sphere-like morphology with mesopores on the surface, observed by field emission scanning electron microscopy (FE-SEM) in Figure 2C,D, respectively. The diameters of MBGNs and CuMBGNs were 142 ± 17 and 128 ± 20 nm, respectively, by statistical analysis from the figures. The content of Cu incorporated in CuMBGN was determined by energy dispersive X-ray (EDS) analysis to be 2.5 at%. After surface amination, the zeta potential of particles increased significantly as seen in Figure 2E. Negative values were measured on MBGNs (−10.4 ± 0.8 mV) and CuMBGNs (−11.2 ± 2.4 mV) whereas positive values were detected on AMBGNs (33.6 ± 2.5 mV) and ACuMBGNs (28 ± 4.8 mV). As further characterized by Fourier transform infrared spectroscopy (FTIR) in Figure 2H, APTES-treated particles showed additional N−H bonds (695 cm⁻¹

ADVANCED
SCIENCE NEWS
www.advancedsciencenews.com

NANO · MICRO
small
www.small-journal.com

vibrations and 1570 cm^{-1} bending mode) compared with those of non-aminated MBGNs. This indicates that aminopropyl moieties were successfully rendered to the particle surfaces which could present potential imine linkages with aldehydes. The morphology of those aminated particles was then observed by SEM, as presented in Figure 2F,G, showing an increasing diameter and large size distribution compared to the nonaminated counterparts. The diameters of AMBGNs and ACuMBGNs were 191 ± 30 and 191 ± 23 nm, respectively, as determined by statistical analysis from the figures.

Ion release was investigated from both CuMBGNs and ACuMBGNs (Figure 2I). Amine-functionalization likely reduces the calcium and silicon release from CuMBGNs during the whole testing period. Particularly, the copper release was significantly restrained before 24 hours (h) of immersion in tris buffer by amine functionalization, compared to non-functionalized CuMBGNs.

2.2. Rheology, Printability, and Self-Healing Properties of the Nanocomposite Hydrogel Inks

Rheological properties including shear thinning, self-recovery properties, and storage/loss moduli of the hydrogels with a variety of compositions were investigated comprehensively to optimize this AG system. First, the rheology of the AG fabricated from various ratios of ADA and GEL (1:1, 1:2, and 1:4) was investigated (Figure S1A–C, Supporting Information). The viscosity of AG inks at low shear rate (0.1 s^{-1}) increased with increasing GEL proportion, implying enhanced shear thinning properties. A higher GEL to ADA ratio also led to the improvement of the yield strength of AG (from 137 to 1500 Pa) and led to increased elastic moduli. In addition, the storage modulus of all samples with different ADA to GEL ratios recovered after sequential high shear rate phases, as shown in Figure S1C in the Supporting Information. Next, the rheology properties of AG with ADA to GEL ratio of 1:4 incorporated with MBGNs, AMBGNs, and ACuMBGNs were compared (**Figure 3**A–C). The introduction of MBGNs into AG led to a decline of elastic moduli and viscosity at low shear rate compared to AG inks, whereas the incorporation of either AMBGs or ACuMBGs could significantly enhance the viscosity and moduli to a similar level, compared to pure AG. All nanocomposite hydrogels showed higher yield strength compared to pure AG, but to a limited level (Figure 3B). All samples performed excellent recovery behavior for their storage moduli (Figure 3C). To study the effect of the amount of AMBGNs added, AG-AMBGN hydrogels were prepared with solid contents of 0.1, 0.5, 1, and 2 w/v% (Figure S1D–F, Supporting Information). Interestingly, the viscosity and elastic modulus increased with increasing solid content from 0.1 to 1 w/v%, while decreased when further increasing the solid content to 2 w/v%. The yield strength increased when the solid content increased to 1 w/v% and declined afterward. As expected, all samples exhibited desirable fast shear recovery behavior.

For the assessment of printability, various printing speeds were tested, and the minimum pressures for maintaining continuous extrusion of strands were applied and fixed for each ink. Figure 3D shows the physical difference between printed strands at different speeds using the 410 µm nozzle. For all the inks, a printing speed of 5 mm s^{-1} led to poorly defined strand structures resulting from too high feed rates. When the printing speed increased to 10 mm s^{-1}, relatively uniform width for individual strand could be obtained. Further increases in printing speed to 20 mm s^{-1} resulted in reduced line widths and discontinuous writing lines with occasional breakage. This behavior indicates that the proper writing speed should be slightly less than or equal to 10 mm s^{-1} for the applied pressure. The optimal extruded strand is shown in Figure S2A (Supporting Information) and the printed thin layers are shown in Figure S2B,C (Supporting Information).

For comparing the shape fidelity of the printed structure by using different inks, ten-layered grid structures with the same porosity were printed (Figure 3D). Generally, all the printed constructs were able to keep their shape. However, differences could be detected when magnifying the partial morphology of the pores using an optical microscope. Relatively angular shapes of pores could be observed on the printed structure using AG inks while the pore size was not uniform with an average of 464 ± 136 µm. Large diffusion of material at the intersections could occur when using the AG-MBGN ink, resulting in the loss of the angular shape of pores and nonuniform pore size (500 ± 59 µm). In contrast, the constructs printed using the AG-AMBGN or ACuMBGN inks retained the angular shape and had more uniform pores with larger size (643 ± 59 and 692 ± 82 µm, respectively), which indicates high printing fidelity. Furthermore, an ear model in centimeter scale was printed as an example of a bionic structure. It can be seen from Figure 3E that the ear models printed using the AG-AMBGN and ACuMBGN inks were more similar to the 3D digital model structurally, in comparison with the ones using AG or AG-MBGN. From the magnified photos in the red box, it can be noticed that the ear models printed using the AG or AG-MBGN inks had a rounder outline and slight differences among the detailed structure compared to those of the digital model. While the ear-shaped structures printed using the AG-AMBGN or ACuMBGN inks almost perfectly matched and kept the detailed structure from the ear model. Scaffolds with 30 layers could be successfully printed by using AG-AMBGN ink, as shown in Movie S1 in the Supporting Information.

The 3D-printed structures showed a rapid self-healing behavior, as presented in **Figure 4**, as a result of the imine bonds obtained via the reaction between ADA, GEL, and aminated surface of particles, as well as the imine bonds formed by Schiff base chemistry.[34] The fabricated ear models using different inks were cut into two halves using a scalpel and then the cut sections were contacted by placing them close to each other. After 4 h of placement in a sealed container at room temperature, self-healing occurred and the two pieces became integrated without separation at the cut/heal position (Figure S3 in the Supporting Information, a dashed box presents the healing interface). These results agree well with the results of the rheology test shown above indicating that G' values of the composite hydrogels were able to recover quickly to the initial values when the strain returned. It is worth noting that here a hydrogel system incorporated with inorganic nanoparticles performed excellent self-healing ability as well, as shown in the Movie S2 in the Supporting Information, indicating that the
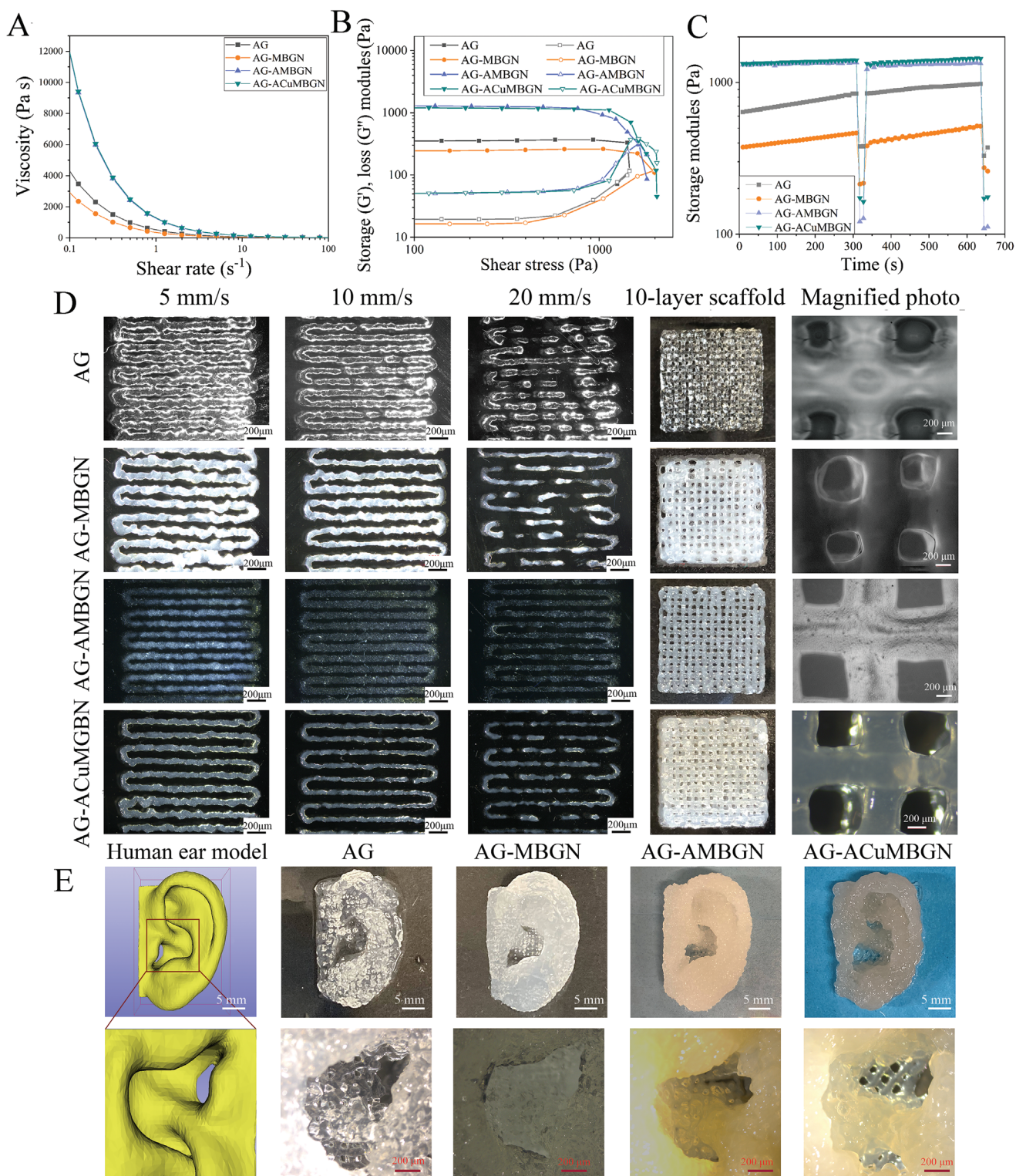
Figure 3. A) Shear thinning properties, B) variations of storage and loss moduli with shear stress, and C) shear recovery properties of AG, AG-MBGN, AG-AMBGN, and AG-ACuMBGN inks, respectively. D) Photographs of printed lines and ten-layer scaffolds at different printing speeds. E) Photographs of printed ear model structures and their magnified images.

healed AG-AMBGN hydrogel showed strong binding ability at the healing interface even under external strain. This behavior could be due to the promising hypothetical benefit of the double crosslinking (Figure 4B) in AG with amine functionalized particles, which could be especially exploited to yield self-healing bionic structures for skeletal tissue engineering.

ADVANCED
SCIENCE NEWS
www.advancedsciencenews.com

NANO · MICRO
small
www.small-journal.com
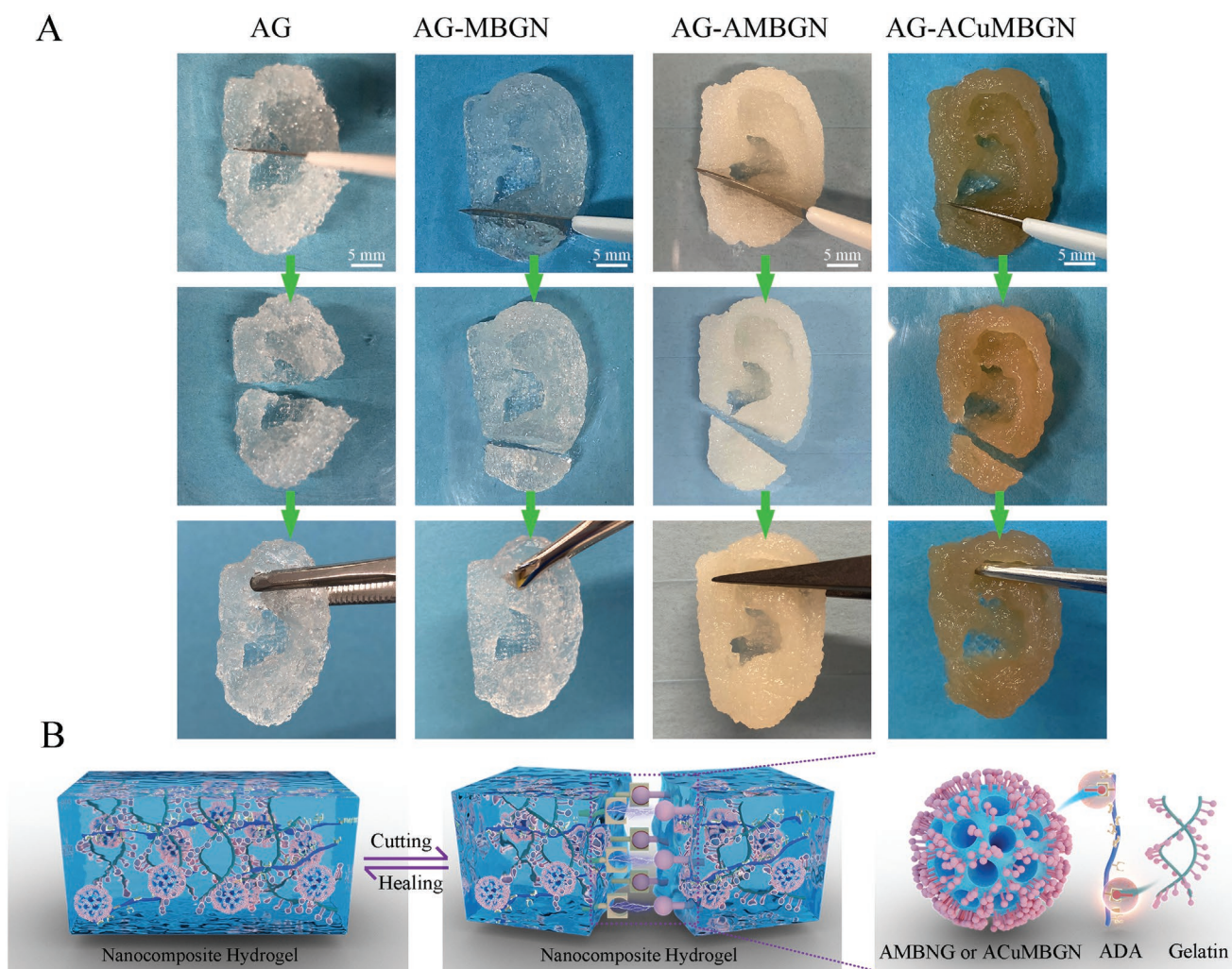
Figure 4. A) Qualitative assessment of self-healing property of printed constructs using different inks. B) Proposed mechanism of self-healing in AG-AMBGN or ACuMBGN hydrogels.

2.3. Microstructure and Physicochemical Property Evaluation of the Nanocomposite Hydrogels

Figure 5A shows FTIR spectra of GEL, ADA, mTG, and ADA-GEL crosslinked with/without mTG. The Schiff base reaction between ADA and GEL could be confirmed by the peak shifts shown at 1522 cm^{-1} (amide II) and 1628 cm^{-1} (amide I) in the spectra of ADA-GEL.[35] In mTG-crosslinked ADA-GEL (ADA-GEL$^+$ mTG), the characteristic peak of mTG could be found at 1076 cm^{-1}, which indicates the residual presence of mTG. Compared to mTG-free ADA-GEL, mTG-crosslinked ADA-GEL also displayed a shifting peak from 1028 cm^{-1} toward lower wavenumbers (1024 cm^{-1}), proving the mTG incorporation inside the hydrogels.[26,35] To clarify the impact of particle addition on the microstructure of those nanocomposite hydrogels, various composite hydrogels after post-crosslinking were freeze dried and observed by SEM (Figure 5B–E). It can be seen that all samples have open and interconnected pore structures. At the particle loading content of 0.5 wt%, the pore distribution looked similar to pure AG (Figure 5B) while the pore sizes of AG-AMBN and

AG-ACuMBGN samples shrank slightly, as can be seen in Figure 5D,E, probably due to an increased interaction among imine linkages in both samples, leading to more condense crosslinking structures. It is worth noting that the mesoporous particles were inclined to agglomerate inside the hydrogel structure (Figure 5C). In contrast, surface functionalized particles were more easily dispersed in the polymers uniformly (Figure 5D,E). FTIR was performed to further investigate the covalent bonding among the four groups, as reported in Figure S4 in the Supporting Information. It was observed that the intensity of peaks in AG-MBGN hydrogels was weaker than that for the other three groups, which may indicate that covalent interactions could be broken by the MBGNs.

Mechanical stiffness before and after post-crosslinking was measured as well, and results are shown in Figure 5F. For both cases, AG nanocomposites with aminated Cu-doped and Cu-free MBGNs retained significantly higher compressive modulus compared to pure AG samples. The modulus of AG-AMBGN and AG-ACuMBGN inks improved by 82% and 77% before post-crosslinking, and by 92% and 68% after post-crosslinking, respectively, compared to AG. On the contrary, AG-MBGN
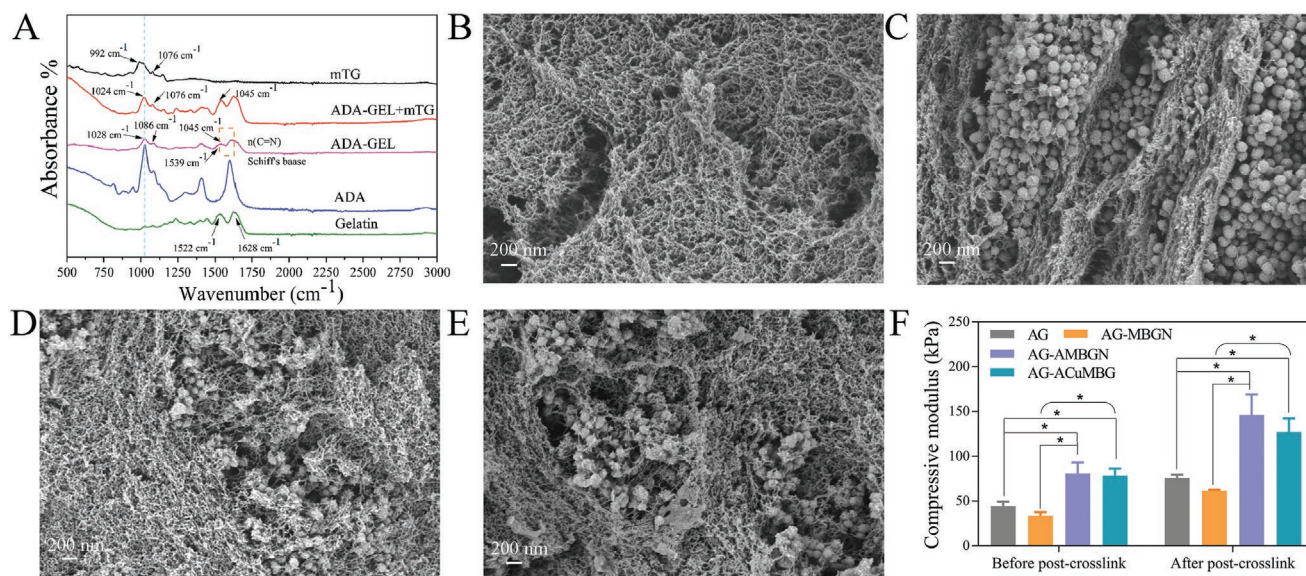
Figure 5. A) FTIR analysis of ADA-GEL hydrogels before and after post-crosslinking. SEM images of B) AG, C) AG-MBGN, D) AG-AMBGN, and E) AG-ACuMBGN samples after post-crosslinking. F) The compressive modulus of the four groups before and after post-crosslinking, $n = 3$, $*p < 0.05$.

samples presented lower modulus (24% and 19% decrease before and after post-crosslinking) than pure AG.

The short/long-term stability of different hydrogels was assessed by a swelling/degradation test, and results are shown in **Figure 6**A. Ionically crosslinked hydrogels presented significantly enhanced swelling capacity until 9 h of incubation and reached their highest swelling ratio as large as 18% for pure AG and 12–14% for the composite hydrogel groups. A subsequent sudden drop of the mass loss was observed for all samples and almost complete dissolution could be obtained at 24 h. In comparison, chemically and ionically crosslinked hydrogel beads (+mTG) showed steadily increasing swelling performance which raised to the maximum (around 7%) at 24 h, and then gradually losing weight until 3 weeks of immersion. As the swelling behavior is indicative of the water content of the swollen hydrogel, lower water content is caused by a less porous network which results from a high crosslinking density. The above results show that the enzymatic and ionically dual-crosslinking process would efficiently increase the crosslinking density of the AG-based systems due to their lower swelling ratio. Regarding the comparison among the different compositions, it can be seen that all the mTG-crosslinked hydrogel disks show similar swelling and degradation trends. However, for the ionically crosslinked hydrogels, incorporation of nanoparticles into AG can significantly suppress its water uptake capability. As a result, the swelling and degradation performance of these nanocomposite hydrogels can be effectively controlled by using an additional post-crosslinking agent, mTG, and the composite hydrogels behaved more stable during long-term incubation compared with the pure ADA-GEL hydrogels.

In vitro biomineralization tests were performed to assess the bioactivity and osteoconductive potential of the nanocomposite hydrogels (Figure 6). After immersion in simulated body fluid (SBF) for 3 days, apatite precipitates could be observed on the AG incorporated with nanoparticles, as seen from the SEM images. The EDS analysis for those precipitations confirms the relative high amount of Ca and P, which are the main components of hydroxyapatite. In comparison, no mineral deposits can be detected on the surface of pure AG after incubation in SBF either from the SEM image or the element analysis. The results reveal thus the bioactive nature of the nanocomposite AG hydrogels in terms of inducing biomineralization in vitro.[36]

2.4. Cell Printing and Bone Tissue Engineering

2.4.1. Human Osteosarcoma Cell Line (MG63) Study

MG63 cells were encapsulated and bioprinted using four different inks and cultured in vitro for 7 days. **Figure 7**A and Figure S3A in the Supporting Information show fluorescence microscope images in the 3D bioprinted scaffolds by live/dead staining on day 1, day 3, and day 7 of culture. The predominant green fluorescence evidences the high viability of cells in all samples (Figure 7A). On day 1, all samples demonstrated high cell viability while most of the cells retained a round shape in all gels, whereas after 3 days of culture, cells exhibiting elongated morphologies could be observed in all groups, and more stretched cells were noted in the AG-AMBGN and AG-ACuMBGN scaffolds. Of note, by day 7, almost all the cells in AG, AG-AMBGN, and AG-ACuMBGN scaffolds exhibited elongated morphology, indicating adequate cellular compatibility and cell proliferation. However, most cells encapsulated in AG-MBGN scaffolds still maintained round shapes and only a few exhibited elongated morphologies.

Indirect viability assessments using the water-soluble tetrazolium salt (WST-8) assay were performed to quantify the cell viability cultured up to day 7 (Figure 7C). It can be seen that MG63 cells showed good proliferation behavior in all groups, suggesting cell compatibility for those ADA-GEL-based inks with addition of various BG nanoparticles.
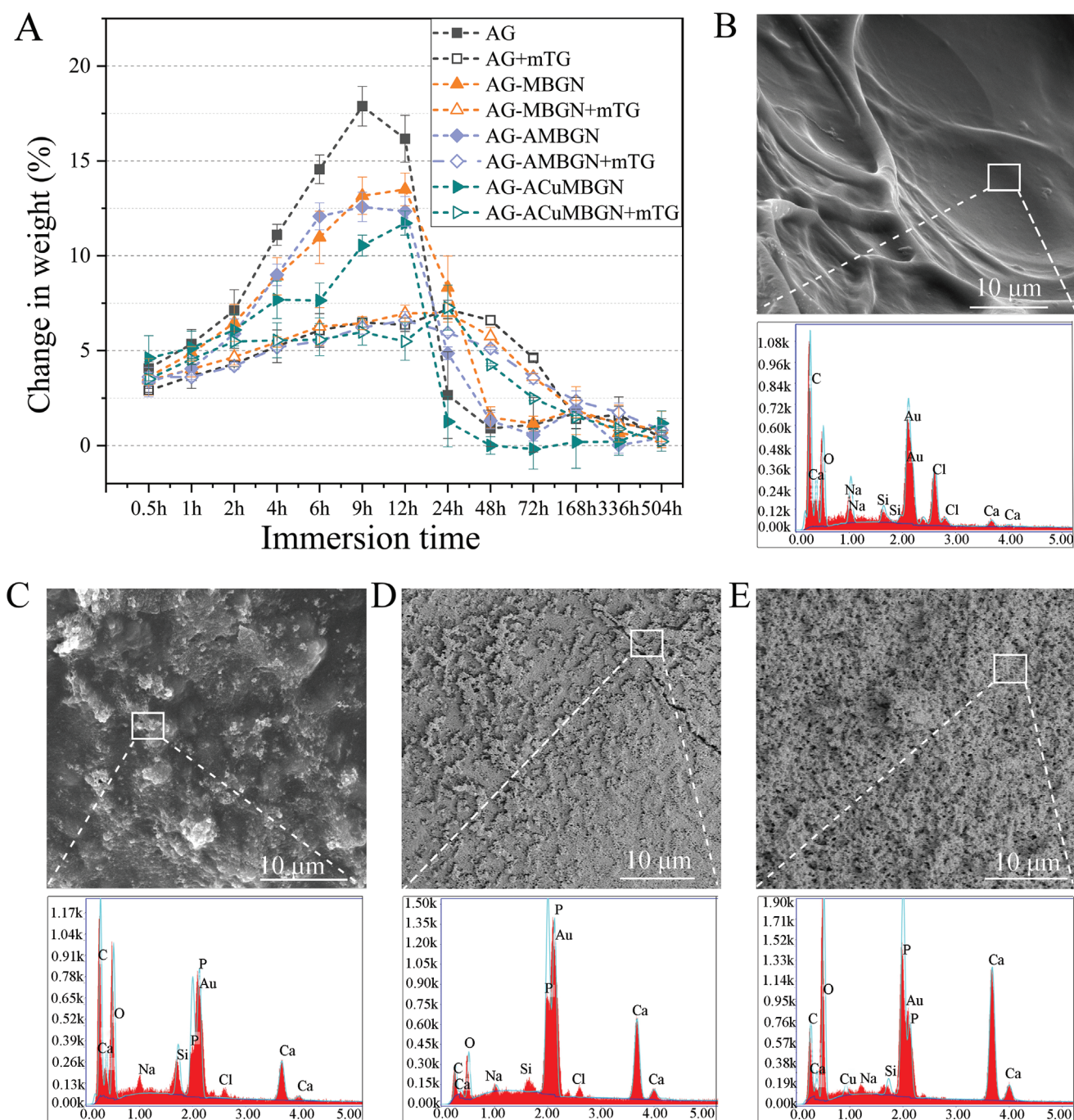
Figure 6. A) Weight changes of lyophilized hydrogel disks over 3 weeks immersion in DPBS at 37 °C ($n = 3$). B–E) SEM images of AG, AG-MBGN, AG-AMBGN, AG-ACuMBGN samples after immersion in SBF for 3 days and results of the element analysis on their surfaces, respectively.

F-actin/DAPI (4′,6-diamidin-2-phenylindol), a major component of the cytoskeleton and nuclei, staining was further carried out to visualize the morphology and spreading of the encapsulated cells in the bioprinted constructs. Figure 7B shows that MG63 cells started to elongate as early as day 1 after extrusion. The elongated cells interweaved with each other spontaneously as the culture time progressed, which can be observed on day 7. Extensive cell spreading took place by day 7 in the bioprinted nanocomposite constructs with NH_2-functionalized MBGNs.

To determine the osteogenic guidance of the nanocomposite bioinks, alkaline phosphatase (ALP) activity of 3D bioprinted constructs at 3 and 7 days is presented in Figure 7D. On day 3, no significant changes in ALP activity were observed in four different groups of constructs. After 1 week of culture, AG-MBGN and AG-AMBGN scaffolds showed a significant increase in ALP activity (*$p < 0.5$) in comparison to the control group. These results suggest that the addition of inorganic BG nanoparticles stimulated osteogenic functionality in AG-based inks.

**ADVANCED
SCIENCE NEWS**

www.advancedsciencenews.com

NANO · MICRO

small

www.small-journal.com
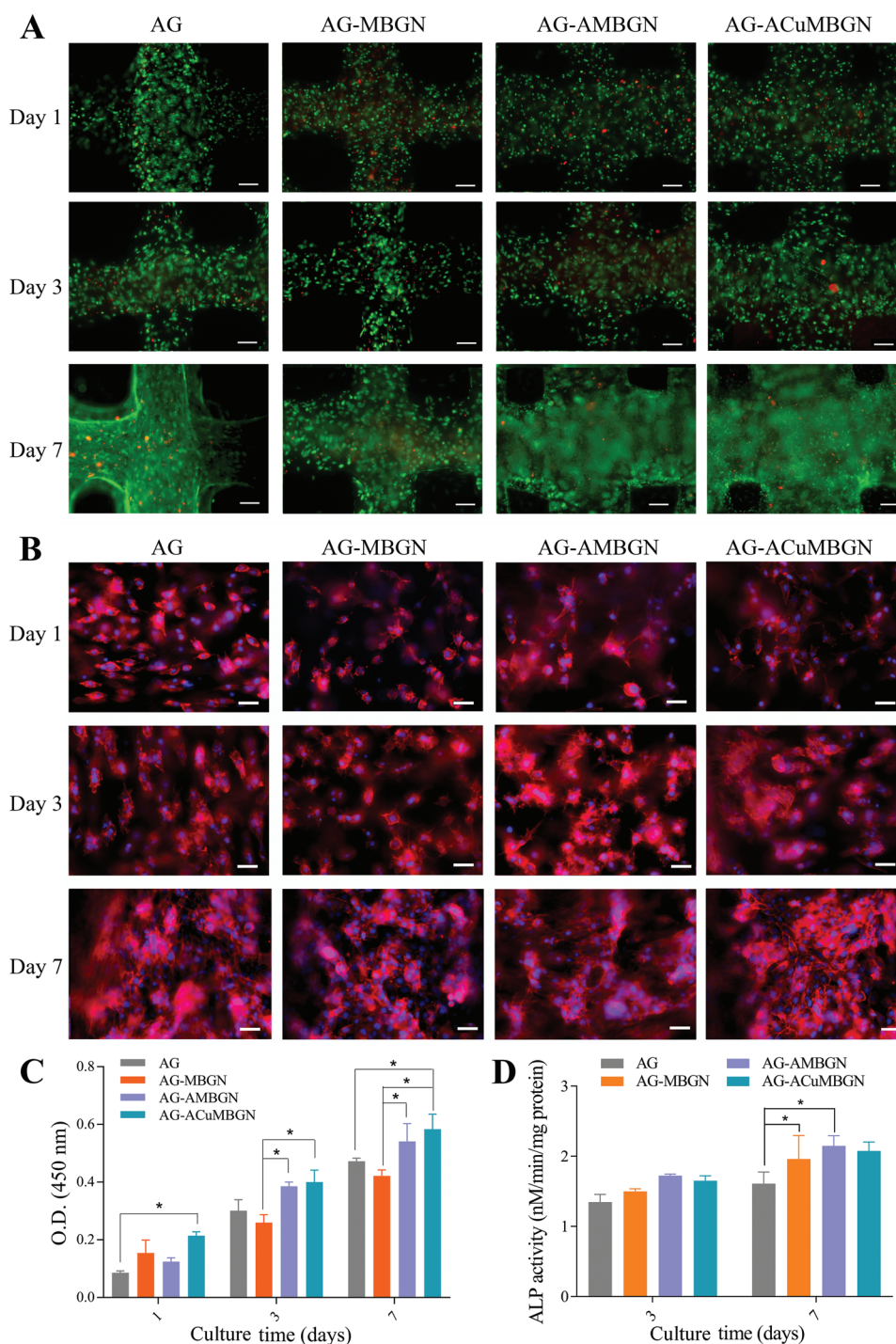
Figure 7. Investigation of MG63 cell performance in bioprinted hydrogels. A) Calcein-AM/phalloindin (PI) live/dead staining images of printed cells observed by fluorescence microscope (scale bar: 200 µm). B) Fluorescence microscopy images of printed MG63 cells stained for F-actin (red) and cell nuclei (blue) after 7 days incubation (scale bar: 50 µm). C) WST-8 tests of bioprinted MG63 cells for 7 days. D) ALP activity of bioprinted MG63 cells after 3 and 7 days of incubation. Statistically significant differences are indicated as: *$p < 0.05$, $n = 3$.

2.4.2. Murine Bone Marrow-Derived Stromal Cell Line (ST2) Study

To verify that nanocomposite bioinks are able to sustain multi-types of osteoblasts with high cell viability and are able to stimulate their angiogenic potential, ST2 cells were encapsulated in

AG and AG-ACuMBGN inks and their biological performance was evaluated on the bioprinted structures.

In **Figure 8**A, the majority of the cells remained viable and only few dead cells were detected in all cases, indicating a high compatibility of both inks with or without ACuMBGNs

ADVANCED
SCIENCE NEWS
www.advancedsciencenews.com

NANO · MICRO
small
www.small-journal.com
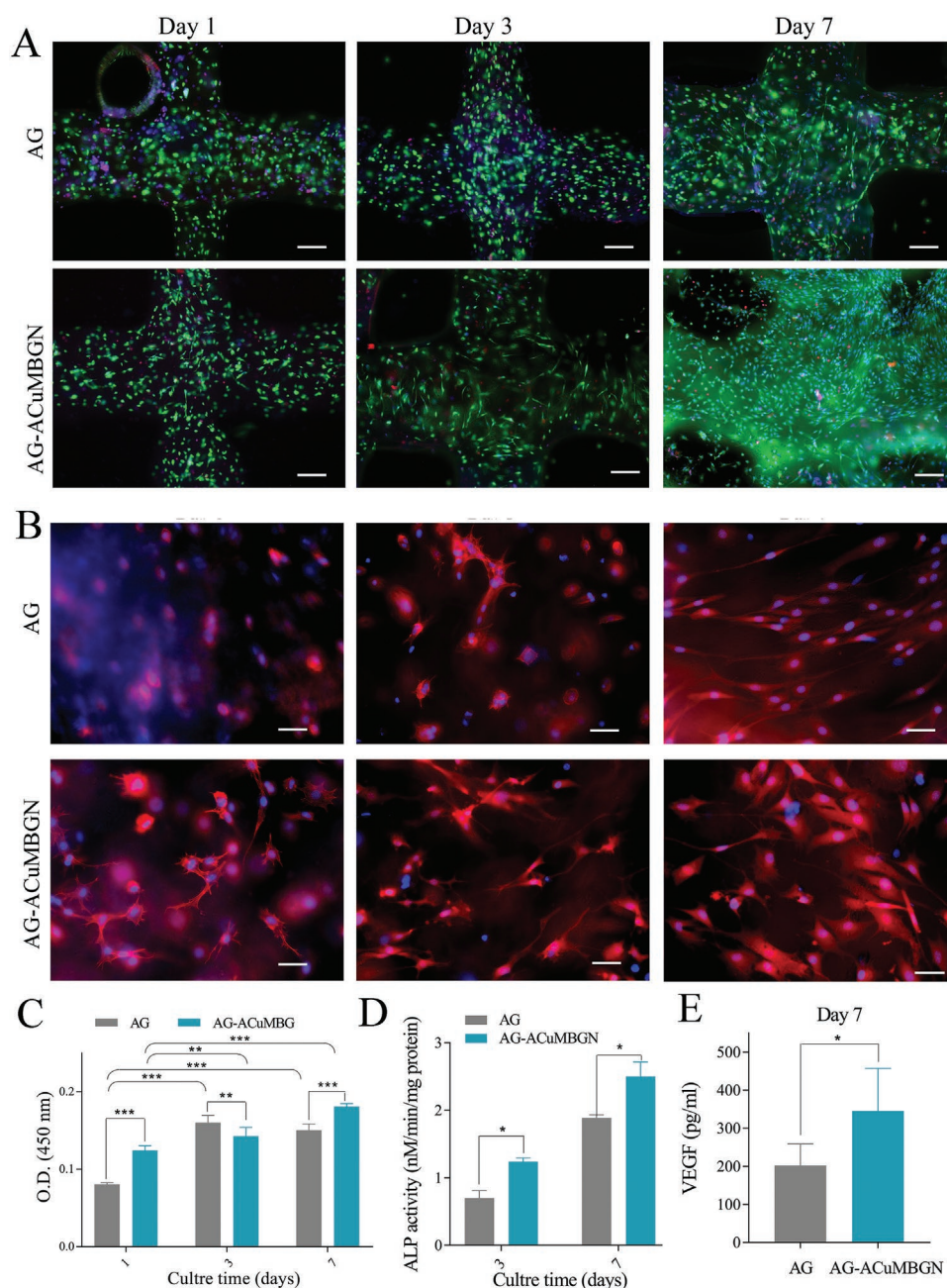
Figure 8. Investigation of ST2 cell performance in bioprinted AG and AG-ACuMBGN hydrogels. A) Calcein-AM/PI live/dead staining images of bioprinted cells observed by fluorescence microscope. All nuclei were stained by Hoechst (scale bar: 200 μm). B) Fluorescence microscopy images of bioprinted ST2 cells stained for F-actin (red) and cell nuclei (blue) after being cultured for 7 days (scale bar: 50 μm). C) WST-8 tests of bioprinted ST2 cells for 7 days. D) ALP activity of bioprinted ST2 cells after 3 and 7 days of incubation. E) VEGF release from the culture medium in bioprinted ST2 cells after 7 days' maturation. Statistically significant differences are indicated as: *$p < 0.05$, **$p < 0.01$, ***$p < 0.001$, $n = 3$.

(Figure S5B, Supporting Information). The printing process did not compromise cell viability as can be seen from Figure 8A at day 1 of the culture period. It is worth noting that cells in AG-ACuMBGN ink started to spread at day 1 and showed better elongated morphologies at each time point, in comparison to hydrogels without particles. Figure 8C shows the quantified results about cell viability and proliferation in both inks by using WST-8 test, suggesting a significant ST2 cell proliferation performance in the printed nanocomposite structures.

In a separate experiment, the bioprinted ST2 cells were stained for F-actin/DAPI within the bioprinted tissue constructs (Figure 8B). As expected, ST2 cells spread well inside all bioprinted structures and a 3D cell–cell network was formed. Notably, the bioprinted AG-ACuMBGN constructs exhibited a marked cell spreading behavior, where cells with stretched morphology were observed even after the first day of printing.

Figure 8D presents the ALP activity of ST2 cells cultured after 3 and 7 days. ACuMBGN-treated bioinks showed a

significantly greater stimulation of ALP activity of ST2 cells (*$p < 0.5$), which is in agreement with the result of the MG63 cell line.

Cu has been known for its promotion of angiogenesis by the secretion of vascular endothelial growth factor (VEGF) from bone marrow stromal cells and for stabilizing the expression of hypoxia-inducible factor (HIF-1α).[37,38] BGs have attracted attention as angiogenic agent due to their relative low cost and high stability compared with growth factor loading strategy.[39,40] To further test the impact of ACuMBGN addition on angiogenesis, we specifically analyzed the release of VEGF from ST2 cells cultured with AG-ACuMBGN and AG-only bioprinted samples. The supernatant was collected from the media in bioprinted scaffolds using both inks and were analyzed for VEGF concentration measured by enzyme-linked immunoassay (ELISA) after 7 days of culture. As seen from Figure 7E, a significantly higher concentration of VEGF was released into the medium in cell-laden ACuMBGN scaffolds compared with pure AG scaffold (*$p < 0.5$).

2.4.3. Primary Stem Cell Study

To further evaluate the osteoblastic and angiogenic differentiation induced by the nanocomposite scaffolds, mouse primary bone marrow stromal stem cells (BMSCs) and primary human umbilical vein endothelial cells (HUVECs) were also encapsulated and printed, respectively. **Figure 9**A shows the 3D live/dead staining image of BMSCs the first day after printing in AG-ACuMBGN hydrogel, indicating the cell viability of printed BMSCs. Figure 9B shows the immunofluorescence of bone morphogenetic protein 2 (BMP2) of the printed BMSCs encapsulated in AG-ACuMBGN hydrogel on day 21. BMP2 is known to play a key role in the osteogenic differentiation of MSC.[41] The positive staining by green-labeled BMP2, together with cell nuclei and cytoskeleton labeled blue and red, respectively, further confirmed the osteoblastic phenotypic maturation of BMSCs in the printed composites. In Figure S6 in the Supporting Information, the BMP2 staining regions in all groups were compared on days 14 and 21. BMP2 was detected in all
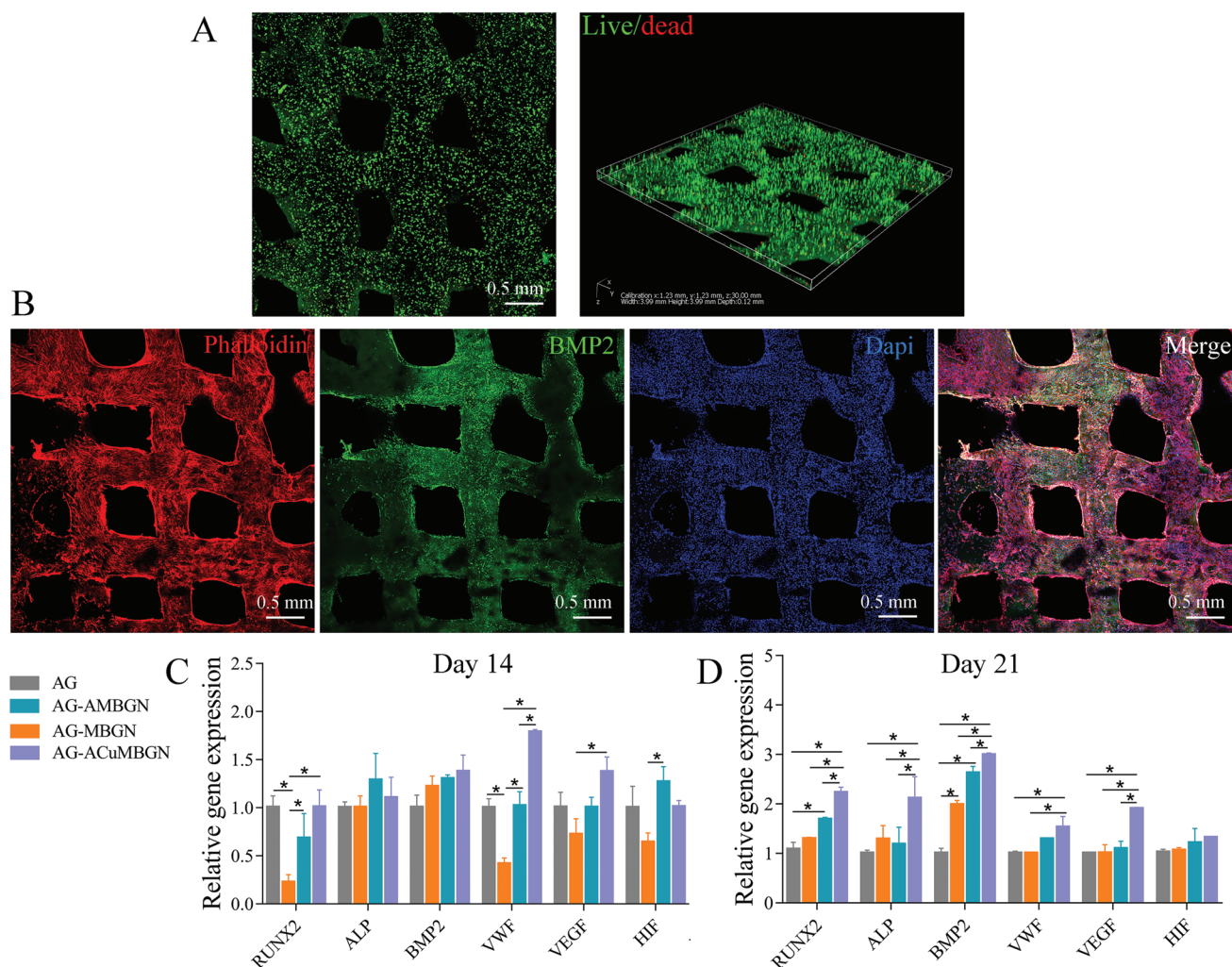
Figure 9. A) Confocal laser scanning microscope (CLSM) images of the live/dead staining of bioprinted BMSCs encapsulated in AG-ACuMBGN inks on day 1. B) Immunofluorescence (scale bar: 0.5 mm) staining of BMP2 (green), cytoskeleton (red), and nuclei staining (blue) on day 21. C,D) Mean mRNA expression levels of osteogenesis-related genes (ALP, RUNX2, BMP2) and angiogenesis-related genes (VWF, HIF, VEGFa) of bioprinted BMSCs on days 14 and 21 by Rt-qPCR analysis,*$p < 0.05$, $n = 3$.

groups at day 14, while obviously larger positive BMP2 staining regions were observed in aminated MBGNs-involved samples. This trend was similar to the immunofluorescence of osteocalcin (OCN), a bone-specific extracellular matrix protein (Figure S7, Supporting Information).[42] OCN expression increased in the scaffolds incorporated with aminated particles. For evaluating the angiogenesis potential of the printed cells, immunofluorescence of VEGF, key regulator of angiogenesis, was performed on the printed BMSC-encapsulated scaffolds in all groups on days 14 and 21 (Figure S8, Supporting Information). Although the presence of VEGF can be detected in all groups, the AG-ACuMBGN group shows a higher expression level. To quantitatively analyze the in vitro osteogenesis and angiogenesis behavior of BMSCs, the relative genes expression was analyzed by real-time quantitative polymerase chain reaction (RT-qPCR) after 14 and 21 days' culture. Figure 9C shows the mean mRNA expression levels of osteogenesis-related genes (ALP, RUNX2, BMP2) and angiogenesis-related genes (VWF, HIF, VEGFa). On day 14, the RUNX2, VWF, VEGFa, and HIF gene expression in AG-ACuMBGN hydrogels was significantly upregulated compared with those in the AG-MBGN group ($*p < 0.05$). However, there was no significant difference in most gene expression values among the four groups. After 21 days, all genes except for HIF were significantly higher expressed in the AG-ACuMBGN group, followed by AG-AMBGN hydrogels. These results are consistent with the staining results and demonstrate that the AG-ACuMBGN hydrogel has the potential to promote the osteogenic differentiation of BMSCs and induce angiogenesis. To further investigate whether copper ions released from AG-ACuMBGN hydrogel were beneficial to the angiogenic effect of HUVECs, CD31 and VEGFa immunofluorescence staining was then performed on the HUVECs-encapsulated AG-ACuMBGN scaffolds, as shown in Figure S9 in the Supporting Information. The VEGF staining area was strongly positive, and the extensive CD31 positive stained regions indicated the potential for new blood vessel formation in the bioprinted AG-ACuMBGN scaffolds.

The above results demonstrated that the present nanocomposite bioink created a favorable microenvironment for encapsulated cells. The ability of such a strategy to simultaneously regulate osteogenic and angiogenic activity has great potential for improving vascularized bone regeneration, as discussed in the next section.

3. Discussion

Despite the significant body of work on extrusion bioprinting applied to bone tissue engineering, enduring challenges remain to refine bioink formulations combining high printing fidelity, optimal microenvironment for cell function, and bone-specific cell signaling cues.[43,44] Many approaches aiming at optimizing the design of bioinks focus on their intrinsically physicochemical properties, especially the rheological properties that can improve the precision and stability of the printed structures. In particular, micro- and nanoparticles,[45] nanofibers,[46] and nanoclay[47,48] have been added as rheological modifiers and viscosity enhancers to improve bioink's mechanical performance. In this

work, we engineered nanocomposite ADA-GEL bioinks not only by optimizing the polymer parameters but also by introducing a double crosslinking network based on reversible imine bonds between the free amino groups both in AMBGN and gelatin with the aldehyde groups in ADA. Sufficient gelation within the pure ADA-GEL hydrogel could be obtained by tuning the appropriate ratio of the amino and aldehyde groups in each sample through adjusting the reactant ratio, as can be seen in Figure S1A–C, Supporting Information. In addition, aminated MBGNs with positive surface charge (confirmed by zeta potential tests) were hypothesized to further form another dynamic covalent bonding between the particles and the hydrogel which provides the ink with enhanced viscosity and storage modulus (Figure 3A–C), enabling holding the ink inside the nozzle without flowing out when in a static state.[49,50] This finding agrees with previous studies, in which aminated silica nanoparticles (NH_2-SiNPs) were incorporated into a polymeric blend of ADA, alginate, and gellan gum to form a bioink.[16] NH_2-SiNPs can be regarded as nanocrosslinkers to bridge the oxidized polysaccharides by imine bond, which can take place in a cell-friendly environment without additional stimuli.[51] It appears that the mechanical properties can be substantially improved in such way with the presence of a relatively low concentration of nanoparticles. However, the drastically increased yield strength (415%) caused by the addition of NH_2-SiNPs was not observed in the work presented here, while the storage modulus was improved significantly (428%) after addition of aminated particles, as can be seen in Figure 3B. Further increasing the AMBGN amount from 0.5 to 2 w/v %, could even reduce the viscosity and modulus (Figure S1D–F, Supporting Information), which is likely the result of the disruption of the crosslinking network by the excess of inorganic fillers.[52,53] Interestingly, the modulus could be completely recovered after removing shear stresses in all groups, indicating excellent self-assembly and self-healing properties induced by the imine linkages. The self-healing ability of hydrogels can be improved by proper chemistry design, high content of functional groups, and selecting proper environmental parameters such as temperature and humidity.[54,55]

As mentioned above, an ideal bioprinted construct should promote cells thriving by providing a biomimetic environment, which means the bioinks have to satisfy the biological requirements associated with the embedded cells. The central issue in the bioprinting field was highlighted by the "biofabrication window" concept proposed by Malda et al.,[56] namely, the need to balance the conflict between the printing forces and their effect on the biological performance of the embedded cells.[49] In this study, the addition of MBGNs did not influence the biocompatibility of the ADA-GEL bioink, and both MG63 and ST2 cells encapsulated in the nanocomposite inks showed viability (Figure S5, Supporting Information) and fast-spreading behavior (Figures 7 and 8). Interestingly, rapid spreading of cells was observed even on day 1 after printing in the AG-AMBGN and AG-ACuMBGN constructs (Figures 7B and 8B). Moreover, faster cell proliferation could be inferred in Figures 7C and 8C. This result can be attributed to the pericellular hydrogel network with dynamic covalent connections of the AG system, which exhibits a strong self-healing ability macroscopically (Figure 5). As it is well known, various cell functions

ADVANCED
SCIENCE NEWS
www.advancedsciencenews.com

NANO · MICRO
small
www.small-journal.com

including proliferation, migration, differentiation, and apoptosis are related to a constant interacting and remodeling of the dynamic ECM.[57,58] Thanks to the reversible nature of imine linkages, the matrix remodeling is allowed in the AG-based hydrogel systems via breakage and reformation of the bonds.[59] Based on a recent study from Yang et al.,[60] this dynamic crosslinking process is able to adapt and reorganize timely in response to cellular forces (shown in Figure 1) and thus facilitates cell spreading in favor of the passing through and extension of cell protrusion structures. Furthermore, the introduced AMBGNs or ACuMBGNs with positively charged surfaces containing -NH_2 exhibit hydrophilic–hydrophobic balance, which is beneficial for protein adsorption and cell adhesion.[61] As a result, those additional cell adhesion features provided to the dynamically responsive AG network can further promote cell mechanosensing for better spreading.[60,62]

Beyond printability and biocompatibility, applications of bioprinting for successful tissue repair involve assuring cell functionality postprocessing and during the maturation stages of the engineered tissue.[63] In the case of regeneration of the skeletal system, the ideal bioink filler is desired to grant cell-instructive properties toward bone formation and vascular growth.[9] To enhance bone regeneration capability of biopolymers for bioprinting, they have been conventionally physically mixed with osteoconductive inorganic materials, or chemically modified with osteogenic molecules.[64] In this work, significantly enhanced enzymatic activity of ALP was detected in scaffolds bioprinted from nanocomposite inks compared with the pure hydrogel ink (Figures 7D and 8D). MBGNs acting as cell signaling cues can deliver biologically active ions such as calcium and silicon to form an induced microenvironment which stimulates osteogenic differentiation, of importance for bone regeneration.[65–68] The use of bioactive ions as biochemical cues has attracted great interest in recent years to improve bone tissue formation by using bioactive additives such as hydroxyapatite (HA),[13,69] tricalcium phosphate (TCP),[70,71] calcium phosphate,[72] and bioactive glasses.[73] Because of the natural similarity to the inorganic component in bones, those Ca-containing fillers are highly applied toward activating the extracellular-signal-regulated kinase (ERK1/2), and thus to upregulate osteogenic differentiation.[74] Furthermore, the introduction of amino groups also has an impact on cell differentiation in 3D, as reported in previous research.[61,75] In addition to the added bioactive stimuli, the physicochemical properties (e.g., stiffness and degradation rate) of the hydrogel network in combination with the dynamic microstructure of the hydrogel matrix play key roles in cell differentiation and tissue formation. As described previously, mesenchymal stem cells' (MSCs) fate can be determined by manipulating the stiffness of the matrix.[76] Huebsch et al.[77] reported that an optimal osteogenic response occurred at an intermediate rigidity of 22 kPa because it is beneficial to the generation of cellular traction forces, neither too soft nor too rigid matrices should be favored for osteogenic differentiation. Likewise, a degradable matrix is desired for osteogenic differentiation in a 3D environment due to the positive impact to generate cellular traction forces.[78] However, the requirements of high printability and shape fidelity for bioinks are normally not in line with the requirement of an optimal microenvironment for adequate cell func-

tion and differentiation, which remains a significant challenge in the field of bioprinting. In this work, the sufficient hydrogel network dynamics, caused by the dynamic crosslinks inside AG and AG with aminated Cu/-MBGNs, could promote cell mechanosensing, resulting in osteogenic differentiation. On the contrary, adipogenesis of encapsulated human MSCs in 3D culture can be facilitated in hydrogels which hinder cell mechanosensing, as reported by Yang et al.[60]

The concept of "angiogenic–osteogenic coupling" was emphasized in recent studies because of the intimate relationship between vascularization and improved bone formation.[27,79] In the current study, Cu^{2+} ions delivered and released by the MBGN carriers are speculated to play a leading role in upregulating VEGF production in the bioprinted nanocomposite constructs in comparison with the pure hydrogel samples. However, a potential synergetic effect of Cu^{2+} in combination with other relevant ions being released such as Ca ions should not be ruled out. The content of Cu^{2+} doped in the CuMBGNs was expected to be in the effective range for angiogenetic applications based on previous reports.[80,81] Further research will be conducted to investigate the potential superiority of the AG-ACuMBGN bioinks to promote vascularization by direct observations of tubule formation, or by in vivo AV-loop model, as discussed previously.[82]

In addition to the above aspects including the mechanics, cell compatibility, and bio-functions of the printed implants, bone tissue scaffolds should replicate the native tissue microstructure and exhibit physicochemical factors such as suitable degradation and mineralization ability which have great impact on developing bioprinted functional bone implants. The bioactive components are released to the surrounding environment in a controlled manner in relation to polymer (matrix) degradation.[83] A suitable degradation rate is essential to provide a favorable environment in which cells can proliferate and express specific marker proteins.[83,84] The current study adopted a dual post-crosslinking strategy for AG using Ca^{2+} ions and mTG, and the weight loss of AG hydrogel samples fell as much as 66% after immersion in Dulbecco's phosphate-buffered saline (DPBS) for 9 h. It has been reported that changing the concentration of the mTG crosslinker solution could further tune the degradation rate of the AG hydrogel.[26,35] Besides, the addition of nanoparticles provides another parameter to keep the long-term stability of the constructs which can be confirmed by the reduced weight loss, as seen in Figure 6. This is because the presence of MBGNs may reduce the space inside the hydrogel network available to host water molecules, which has been reported previously.[85,86] As for the functionalized MBGNs-incorporated AG hydrogels, the particle–polymer interactions can be increased due to more intense covalent linkages based on Schiff-base reaction, which can prevent hydrogel degradation and swelling. On the other hand, the hydrophobic character caused by the amino groups on particle surface would further avoid water uptake.[85]

Moreover, the bioactivity (biomineralization ability) of bioinks refers to the creation of a microenvironment mimicking host bone tissue. As can be seen in Figure 6, apatite deposition can be detected on the printed nanocomposite hydrogel constructs (AG-MBGN/AMBGN/ACuMBGN) after immersion in SBF for 3 days, while no mineralization developed on the pure

AG sample surface, indicating the improved bioactivity performance of the samples via incorporation of BGNPs. The bioactive microenvironment will further stimulate the osteogenic activity of the encapsulated cells.[87,88] This result is consistent with previous reports on BG-containing polymer systems.[25]

Nanoparticle-hydrogel composites exhibit multifunctional and self-healing properties, which make them attractive to develop "smart" materials.[89] Such materials can potentially be used to engineer tissue–implant interactions and to develop advanced therapeutic approaches, especially for tissue reconstruction and regeneration.[90,91] This study developed nanocomposite bioinks integrating self-healing capacity, shape fidelity, adjustable degradation performance, bioactivity and biocompatibility. Further multibiofunctionalities were imparted by the ions Ca^{2+}, Si^{4+}, and Cu^{2+}) releasing capability of the incorporated MBGNs, enhancing interactions among cells and cell response, which represents a suitable approach for developing a new generation of bioinks incorporating bioactive fillers.

4. Conclusions

Amino-functionalized MBGNs with and without Cu ions were introduced into ADA-GEL hydrogels to create a novel nanocomposite formulation. The printability of nanocomposite bioinks and the fidelity and precision of the printed constructs were improved by involving the additional dynamic imine linkages between the nanoparticles and the hydrogel. The addition of BGNPs significantly endows the printed constructs with superior bioactivity and long-term stability. By adopting a simultaneous enzyme and ion dual crosslinking approach, it is possible to control the degradation behavior of the bioprinted samples. More importantly, the dynamically bioink matrix crosslinked with imine bonds between both hydrogel molecules and aminated particles has an impact on facilitating cell proliferation, cell spreading, and osteogenic differentiation. Together with the biological functionality brought by ACuMBGNs, the developed nanocomposite bioink showed osteogenic and angiogenic effects. Based on these favorable properties, the new multifunctional nanocomposite bioinks may expedite the applications of 3D-printed cell-laden structures in bone tissue engineering.

5. Experimental Section

Materials: Copper chloride $CuCl_2·2H_2O$ (≥99.99%), L-ascorbic acid (≥99%), cetrimonium bromide (CTAB, ≥ 97%), ethyl acetate (EA, ≥99.8%), tetraethyl orthosilicate (TEOS, ≥99.0%), gelatin (from porcine skin, Bloom 300, Type A), 3-aminopropyl triethoxy silane (APTES, $H_2N(CH_2)3Si(OC_2H_5)_3$), and toluene were purchased from Sigma-Aldrich, Germany. Sodium alginate PH 163 S2 (MW 100 000–200 000 g mol^{-1}, guluronic acid content 65–70%) was obtained from JRS Pharma GmbH & Co. KG, Germany. Calcium nitrate tetrahydrate (≥99.4%, VWR) ammonia solution (1 M, VWRSodium metaperiodate ($NaIO_4$), calcium chloride di-hydrate ($CaCl_2·2H_2O$), and ethylene glycol were purchased from VWR international, Germany. Dialysis tubes (MWCO: 6–8 kDa) were purchased from Repligen (Waltham, USA). Propidium iodide (PI), Calcein AM, Rhodamine phalloidin, Hoechst, and DAPI were purchased from Thermo Fisher Scientific™. If not otherwise noted, all other chemicals were purchased from Sigma Aldrich.

Fabrication of Amino-Functionalized MBGNs and CuMBGNs: Cu/ascorbic acid complex was prepared first as reported in the literature.[92]

Briefly, $CuCl_2·2H_2O$ (≥99.99%, Sigma-Aldrich) was first dissolved in 50 mL of deionized water and then heated at 80 °C under magnetic stirring for 1 h. After that, L-ascorbic acid (≥99%, Sigma-Aldrich) aqueous solution was dropwise added to the $CuCl_2$ solution, followed by further reaction for 24 h at 80 °C under stirring. Then the mixture was centrifuged at 7000 rpm for 20 min and the supernatant, composed of Cu/ascorbic acid complex suspension, was stored in a fridge (4 °C) for further use. MBGNs (binary composition of 85% SiO_2–15% CaO in mol.%) were prepared using a microemulsion-assisted sol–gel method reported previously.[92] Briefly, 8 mL of ethyl acetate was dissolved in 26 mL of aqueous solution of CTAB (20% w/v) under stirring for 30 min. Then 5.6 mL of ammonia solution was added and stirred for another 30 min. Then 2.88 mL of TEOS and 1.83 g of $Ca(NO_3)_2$ were sequentially added at an interval of 30 min. For synthesizing Cu-dopped MBGNs, 7 mL of Cu/ascorbic acid complex was added to the mixture. After another 4 h stirring, the products were centrifuged at 7197 rcf for 20 min, washed three cycles with DIW/ethanol, and dried at 60 °C overnight. Finally, the powders were calcined at 700 °C for 4 h with a heating rate of 2 °C min^{-1}. The synthesized products were denoted as MBGNs and CuMBGNs, respectively. The calcined nanoparticles were amino-functionalized by a post-process procedure.[93] Briefly, 100 mg of nanopowder and 2 vol% of APTES were added in 40 mL of anhydrous toluene under refluxing and stirring at 80 °C for 6 h. After that, the products collected were washed with toluene by centrifugation, and finally dried at 80 °C for 3 days.

Fabrication of Oxidized Alginate, Nanocomposite Hydrogel Disks, and Inks: ADA was synthesized as described elsewhere.[30,94] Briefly, 10 g of sodium alginate was dispersed in 50 mL of ethanol under stirring. Then 50 mL of aqueous solution of $NaIO_4$ (6.416% w/v) was added under stirring at room temperature (RT) for 6 h. After that, 10 mL of ethylene glycol was added to quench the reaction followed by another 30 min stirring. The products were then dialyzed against ultrapure water for 5 days with water change daily. It is worth noting that all the oxidation process was in the absence of light. Finally, the resulting ADA solution was purified, frozen, and lyophilized (Alpha 1–2 LD plus, Martin Christ, Osterode am Harz, Germany) to obtain the ADA products. The oxidation degree of ADA was ≈30%, determined as reported previously.[95,96] Gelatin and ADA solutions were obtained by dissolving 12% w/v of GEL powder and 3% w/v of solid ADA in DPBS solution at 37 °C and RT, respectively. For preparing pure ADA-GEL(AG), ADA solution was added dropwise into GEL solution under continuous stirring to obtain an AG precursor mixture; for preparing nanocomposite ADA-GEL incorporated with nanoparticles, the nanoparticles were first added to ADA solution to obtain a homogenous dispersion under stirring and ultrasonication, and then transferred to GEL solution to produce AG-MBGN/AMBGN/ACuMBGN mixtures. After that, the precursor mixture was quickly transferred into silicone molds (Ø 9 mm × 4 mm or Ø 20 mm × 1 mm), and hydrogels could be formed after 10–20 min gelation. A post-crosslinking process was carried out by immersing the hydrogel disks into 0.1 M $CaCl_2$ solution supplemented with 2.5 w/v % of mTG. The inks were formed by simply transferring the precursor mixture into cartridges and leaving them to react for 10–20 min at RT before using them for printing.

Rheology Tests: The rheological characterization was done using a DHR3 rheometer (TA-Instruments Ltd., USA) at RT with a gap distance of 0.5 mm. Hydrogel samples were made in silicon mold (Ø 20 mm × 1 mm) and left to stay for 4 h, without post-crosslinking process as it was intended to investigate the rheology of the inks. The shear-thinning properties were characterized by recording the viscosity with the logarithmically increasing shear rate in a range of 0.01–100 s^{-1}. The storage (G') and loss (G'') moduli were tested at a range of shear strength from 0.1 to 10 000 Pa. The crossover point of G' and G referred to yield strength. The shear recovery properties were assessed by measuring G' and G'' with 0.5% strain at the frequency of 1 rad s^{-1} for 5 min, followed by the measurement with 500% strain for 10 s at the same frequency.

Physico-Chemical Characterization: The amorphous structure of the synthesized MBGNs and CuMBGNs was tested by XRD analysis (Rigaku, MiniFlex 600, Japan) in the 2θ range of 10°–70° and step size of 0.020°.

The morphology of MBGNs and CuMBGNs was observed by FE-SEM (Auriga, Carl Zeiss). EDS analysis (X-MaxN, Oxford Instruments) was performed to analyze the chemical composition of Cu-MBGNs. Particle size distribution was analyzed by Nano Measurer 1.2 software and at least 40 particles were measured. To confirm the successful amination of the particles, the zeta potential of MBGNs, AMBGNs, and ACuMBGNs was measured in aqueous phase using a Zetasizer Nano ZS (Malvern Instruments, UK) instrument with a 4 mW HeNe laser (633 nm) and a light scattering detector positioned at 90°, respectively. The chemical analysis of the freeze-dried hydrogel films was performed by FTIR (IRAffinity-1S, Shimadzu) over a range of 3000 to 500 cm^{-1}. The microstructure of AG w/o particles after post-crosslinking was observed by SEM as well. The ion release behavior of CuMBGNs and ACuMBGNs was analyzed in Tris-buffer (Trizma R Pre-set crystals, Sigma-Aldrich, pH 7.4). Briefly, 10 mg of particles were soaked in 20 mL of Tris-HCl solution in an incubator at 37 °C for up to 3 days. At each predetermined time point, the samples were centrifuged and 5 mL of the supernatant was collected and replenished with fresh 5 mL of fresh Tris solution. The ionic concentration of the supernatant was analyzed by using inductively coupled plasma-mass spectrometry (NexION 350 PerkinElmer, US).

Compression tests were carried out using a texture analyzer (Stable Micro Systems, London, England) at a compression speed of 0.01 mm s^{-1} for hydrogel disks with and without post-crosslinking in a solution containing 0.1 M CaCl$_2$ and 2.5 w/v % mTG. Hydrogel disks with 4 mm in thickness and 9 mm in diameter were used for compression tests. The moduli were calculated from the slope of the stress–strain curves of hydrogels in the linear-elastic range.

Mass loss and swelling tests were done following the protocol described previously.[26] Briefly, sample disks ($n = 3$) were fabricated with material composition of pure AG, AG-MBGN, AG-AMBGN, and AG-ACuMBGN hydrogels. After post-crosslinking, those samples were lyophilized to obtain their dry weights (w_d, $t = 0$). Then all samples were immersed into DPBS at 37 °C. The weight of the samples was recorded at each timepoint up to 3 weeks and denoted as wet weight (W_w). The swelling ratio (SR) was calculated by the following equation

$$SR(\%) = \frac{W_w - W_d}{W_d} \times 100\% \qquad (1)$$

The bioactivity of all dried samples was evaluated by immersing in SBF at 37 °C for 3 days. SBF was prepared following the protocol described by Kokubo.[28] Samples were rinsed with distilled water and lyophilized for SEM analysis.

3D Printing: The 3D printing process was performed using an extrusion-based 3D printer (type BioScaffolder 3.1, GeSiM, Germany). The scaffolds were printed as orthogonal grids with 15 struts per layer and an edge length of 15 mm. The typical printing pressure ranges were 110–120 kPa for the AG ink, 90–100 kPa for the AG-MBGN ink, and 130–140 kPa for AG-AMBGN/ACuMBGN inks. Printing speed in the range of 7–9 mm s^{-1} and a needle with a diameter of 410 mm were used. A stereo microscope (ZEISS, Stemi 508, Germany) was adopted to observe the printed constructs. For printing cells, another extrusion-based 3D printer (BioScaffolder 3.1, GeSIM, Radeberg, Germany) installed in a sterile bench was used. The bench with the printer was sterilized by UV irradiation for 1 h before use. For the preparation of bioinks, the cells were encapsulated into different groups of hydrogels yielding a final cell concentration of 1×10^6 cells mL^{-1} and then transferred to sterilized cartridges waiting to be used. The cell-laden scaffolds were printed and then post-crosslinked in a solution containing CaCl$_2$ (0.1 M) and mTG (0.025 g mL^{-1}) for 10 min, followed by washing twice with Hanks' balanced salt solution (HBSS) and cultured in the incubator at 37 °C with 5% CO$_2$.

Self-Healing Tests: The printed ear models or hydrogel disks using the four different types of inks were cut using a scalpel. Then they were piled up again and placed in sealed plastic dishes at RT. After 4 h healing without any external pressure or stimuli, the ear models were clipped up and the hydrogel was pulled with tweezers to observe whether they were self-healable.

Cell Study: For cell culture studies, human osteosarcoma cell line MG63, murine bone marrow-derived stromal cell line ST2 (German Collection of Microorganisms and Cell culture, Germany), mouse primary bone marrow stromal stem cells (BMSCs, Air Force Medical University, China), and human umbilical vein endothelial cells (HUVECs, Sciencell Co., Ltd., China) were used. MG63 cells (passage 10–20) were cultured in a growth medium (GM) containing DMEM (Dulbecco's modified Eagle medium, Thermo Fisher Scientific, USA) supplemented with 10% fetal bovine serum (FBS, Corning, USA) and 1.0% penicillin-streptomycin (PS, Thermo Fisher Scientific, USA) at 37 °C, 95% humidity, and 5.0% CO$_2$ in an incubator. Cell pellets were collected for preparing bioinks as follows: cells were digested with 0.25% Trypsin-EDTA (Thermo Fisher Scientific, USA) and collected after being centrifuged at 1000 rpm for 5 min. Then cells were resuspended in DPBS and counted using Neubauer chambers (Neubauer improved, Paul-Marienfeld, Germany). After that, the desired amount of cells was centrifuged again to obtain the cell pellets. 3D bioprinted constructs were cultured in the same GM for 1, 7, and 14 days in the incubator.

The viability of MG63 cells was assessed by live/dead staining tests. Cell-laden scaffolds were washed and incubated in HBSS containing 4 µL mL^{-1} Calcein AM and 1 µL mL^{-1} PI for 45 min in a cell incubator. Live (green) and dead (red) cells in scaffolds were visualized by taking images using fluorescence microscope (AxioScope A.1, Carl Zeiss, Germany). The survival rates of cells were calculated by dividing living cell numbers by total cell numbers, which were counted using Image-J.[97] Water-soluble tetrazolium salt (WST-8) assays were applied on the tripartite samples to evaluate the metabolic activity of the printed cells. After incubating in GM with 1% WST-8 solution for 3 h at 37 °C, 100 µL of the supernatant was transferred into 96-well plates, followed by reading their absorbance at 450 nm using a well plate reader (type Phomo, Anthos Mikrosysteme GmbH, Krefeld, Germany). In order to visualize F-actin structures within cells after bioprinting, cells were first fixed using a fixing solution composed of 4% w/v polyethylene glycol (PEG), 1×10^{-3} M ethylene glycol tetraacetic acid (EGTA), 3.7% (w/v) paraformaldehyde, and 100×10^{-3} M piperazine-N,N′-bis(2-ethanesulfonic acid/PIPES in HBSS. Then F-Actin and nuclei of cells were stained with Rhodamine Phalloidin (Thermo Fisher Scientific, USA) and DAPI (Invitrogen, France), and then the samples were imaged by FM. To analyze the osteogenic behavior of printed cells, alkaline phosphatase (ALP) activity was quantified after 1 week culture. Briefly, the cells were released from the printed samples immersing the scaffolds in 0.25% Trypsin-EDTA in an incubator for 10 min, then centrifuged and washed with PBS to remove the remaining Trypsin, resulting in cell pellets. Subsequently, samples were lysed by a lysis buffer (pH 7.5) containing 10×10^{-3} M Tris-HCl, 1×10^{-3} M MgCl$_2$, and 0.05% Triton X-100. The enzyme activity was determined using 0.1×10^{-3} M para-nitrophenyl phosphate (pNPP) as a substrate in an assay buffer containing 0.1 M Tris and 1×10^{-3} M MgCl$_2$ (pH 10.0 Sigma-Aldrich). The reaction was stopped after incubation at RT for 30 min by adding NaOH solution. The absorbance was read at 405 and 690 nm by UV-vis spectrophotometer (Specord 40, Analytic Jena AG, Germany). The total protein content was determined by using bovine serum albumin (BSA) as a standard. Samples were measured in triplicate. The ALP activity was presented as the amount of p-nitrophenol produced by cells per minute and milligram of total protein.

ST2 cells (passage 6–15) were cultured in GM containing RPMI 1640 (Mammalian Cell Culture Medium, Thermo Fisher Scientific, USA) supplemented with 10% FBS and 1.0% PS, at 37 °C, 95% humidity, and 5.0% CO$_2$ in an incubator. For the process of bioink preparation, WST assay, and F-actin/DAPI staining were the same as when using MG63 cells. Cells were stained with 4 µL mL^{-1} Calcein AM, 1 µL mL^{-1} PI, and 4 µL mL^{-1} Hoechst for live/dead staining test. VEGF-A release in the surrounding cell culture medium was measured on day 7 for investigating possible angiogenesis effects of the nanocomposite hydrogel scaffolds. The medium exchange was performed every other day during the culture period. A mouse VEGF Elisa Kit (RayBiotech, Inc., USA) was used according to the manufacturer protocol and the optical density at 450 nm was read by a plate reader for the quantification of VEGF release.

ADVANCED
SCIENCE NEWS

www.advancedsciencenews.com

NANO · MICRO
small
www.small-journal.com

BMSCs (passage 3–5) were cultured in medium (No. BDMF-03011, Cyagen Biosciences Co., Ltd., China) supplemented with fetal 5% bovine serum and 1% penicillin (No. MUXMX-05001, Cyagen), at 37 °C, 95% humidity, and 5.0% CO_2 in an incubator. HUVECs were cultured in endothelial culture medium (No. 1001, Sciencell) containing 5% FBS (No. 0025), 1% endothelial cell growth supplement (No. 1052), and 1% penicillin/streptomycin solution (No. 0503) in 5% CO_2 at 37 °C. The process of bioink preparation and F-actin/DAPI staining was the same as when using MG63 cells.

For immunofluorescence (IF) staining, bioprinted constructs at day 14 and day 21 were fixed in 4% formalin followed by washing three times with DPBS and cell permeabilization treatment in 0.25% Triton X-100 in PBS. Cells were washed and then incubated in 5% BSA for 30 min. After the washing step, cells were incubated with the primary antibody (1:100, monoclonal mouse, Santacruz) in the staining solution overnight at 4 °C. After washing the samples with fresh staining solution, cells were incubated in FITC-labeled normal mouse IgG secondary antibody (1:100, Santacruz) in staining solution for 1 h. Samples were then stained with phalloidin and DAPI to visualize F-actin and cell nuclei, respectively. Cells were imaged by using a confocal laser scanning microscope (CLSM, Nikon). All collected images were processed using ImageJ (NIH, Bethesda, MD, USA) for further analysis.

The osteogenic differentiation-related gene (RUNX2, ALP, and BMP2) expression and angiogenesis related gene (VWF, VEGF and HIF) expression were analyzed by RT-qPCR after incubation for 14 and 21 days. Briefly, the cells were harvested, and the total RNA was isolated using pellet pestles and RNAfast1000 Total RNA Extraction Kit (Xianfeng Biotechnology, Co., Ltd., China) according to the manufacturer's instructions. cDNA was then synthesized using PrimeScript cDNA Synthesis Kit (Takara Bio Inc., Japan). RT-qPCR was performed using a Maxima SYBR Green/ROX qPCR kit (Thermo Scientific) and conducted on a Quantstudio 6 Flex (Life technologies). Each gene was run in duplicate in a single plate, and the gene expressions were calculated by the 2−ΔΔCt method. The results were normalized to the expression of house-keeping gene GAPDH. The primer sequences and genes are presented in Table S1 in the Supporting Information.

Statistical Analysis: All data were reported as mean and standard deviation (SD). Two-way analysis of variance followed by Bonferroni's multiple comparison tests were applied for statistical analysis by using GraphPad Prism 7. The significances were set as $*p < 0.05$, $**p < 0.01$, $***p < 0.001$.

Supporting Information

Supporting Information is available from the Wiley Online Library or from the author.

Acknowledgements

Conflict of Interest

The authors declare no conflict of interest.

Data Availability Statement

The data that support the findings of this study are available from the corresponding author upon reasonable request.

[1] A. C. Daly, M. E. Prendergast, A. J. Hughes, J. A. Burdick, *Cell* **2021**, *184*, 18.

[2] L. Ouyang, in *Study on Microextrusion-Based 3D Bioprinting and Bioink Crosslinking Mechanisms* (Ed: L. Ouyang), Springer Singapore, Singapore **2019**, pp. 7–23.

[3] I. T. Ozbolat, M. Hospodiuk, *Biomaterials* **2016**, *76*, 321.

[4] X. Li, B. Liu, B. Pei, J. Chen, D. Zhou, J. Peng, X. Zhang, W. Jia, T. Xu, *Chem. Rev.* **2020**, *120*, 10793.

[5] W. L. Ng, J. M. Lee, M. Zhou, Y. W. Chen, K. A. Lee, W. Y. Yeong, Y. F. Shen, *Biofabrication* **2020**, *12*, 022001.

[6] W. Sun, B. Starly, A. C. Daly, J. A. Burdick, J. Groll, G. Skeldon, W. Shu, Y. Sakai, M. Shinohara, M. Nishikawa, J. Jang, D.-W. Cho, M. Nie, S. Takeuchi, S. Ostrovidov, A. Khademhosseini, R. D. Kamm, V. Mironov, L. Moroni, I. T. Ozbolat, *Biofabrication* **2020**, *12*, 022002.

[7] P. S. Gungor-Ozkerim, I. Inci, Y. S. Zhang, A. Khademhosseini, M. R. Dokmeci, *Biomater. Sci.* **2018**, *6*, 915.

[8] J. Zhang, H. Eyisoylu, X.-H. Qin, M. Rubert, R. Müller, *Acta Biomater.* **2021**, *121*, 637.

[9] G. Cidonio, C. R. Alcala-Orozco, K. S. Lim, M. Glinka, I. Mutreja, Y.-H. Kim, J. I. Dawson, T. B. F. Woodfield, R. O. C. Oreffo, *Biofabrication* **2019**, *11*, 035027.

[10] A. Habib, B. Khoda, *J. Manuf. Processes* **2019**, *38*, 76.

[11] S. Heid, A. R. Boccaccini, *Acta Biomater.* **2020**, *113*, 1.

[12] N. Di Marzio, D. Eglin, T. Serra, L. Moroni, *Front. Bioeng. Biotechnol.* **2020**, *8*, 326.

[13] A. Wenz, K. Borchers, G. E. M. Tovar, P. J. Kluger, *Biofabrication* **2017**, *9*, 044103.

[14] R. Michel, R. Auzély-Velty, *Biomacromolecules* **2020**, *21*, 2949.

[15] F.-F. Cai, S. Heid, A. R. Boccaccini, *J. Biomed. Mater. Res., Part B* **2021**, *109*, 1090.

[16] M. Lee, K. Bae, C. Levinson, M. Zenobi-Wong, *Biofabrication* **2020**, *12*, 025025.

[17] G. Choe, S. Oh, J. M. Seok, S. A. Park, J. Y. Lee, *Nanoscale* **2019**, *11*, 23275.

[18] N. Zandi, E. S. Sani, E. Mostafavi, D. M. Ibrahim, B. Saleh, M. A. Shokrgozar, E. Tamjid, P. S. Weiss, A. Simchi, N. Annabi, *Biomaterials* **2021**, *267*, 120476.

[19] M. Lee, K. Bae, P. Guillon, J. Chang, Ø. Y. Arlov, M. Zenobi-Wong, *ACS Appl. Mater. Interfaces* **2018**, *10*, 37820.

[20] S. M. Bakht, A. Pardo, M. Gómez-Florit, R. L. Reis, R. M. A. Domingues, M. E. Gomes, *J. Mater. Chem. B* **2021**, *9*, 5025.

[21] F. L. C. Morgan, L. Moroni, M. B. Baker, *Adv. Healthcare Mater.* **2020**, *9*, 1901798.

[22] N. Li, R. Guo, Z. J. Zhang, *Front. Bioeng. Biotechnol.* **2021**, *9*, 630488.

ADVANCED
SCIENCE NEWS

www.advancedsciencenews.com

NANO · MICRO
small
www.small-journal.com

[23] R. Levato, T. Jungst, R. G. Scheuring, T. Blunk, J. Groll, J. Malda, *Adv. Mater.* **2020**, *32*, 1906423.

[24] L. Shang, Z. Liu, B. Ma, J. Shao, B. Wang, C. Ma, S. Ge, *Bioact. Mater.* **2021**, *6*, 1175.

[25] Á. J. Leite, B. Sarker, T. Zehnder, R. Silva, J. F. Mano, A. R. Boccaccini, *Biofabrication* **2016**, *8*, 035005.

[26] S. Schwarz, S. Kuth, T. Distler, C. Gögele, K. Stölzel, R. Detsch, A. R. Boccaccini, G. Schulze-Tanzil, *Mater. Sci. Eng., C* **2020**, *116*, 111189.

[27] E. J. Ryan, A. J. Ryan, A. González-Vázquez, A. Philippart, F. E. Ciraldo, C. Hobbs, V. Nicolosi, A. R. Boccaccini, C. J. Kearney, F. J. O'Brien, *Biomaterials* **2019**, *197*, 405.

[28] L. B. Romero-Sánchez, M. Marí-Beffa, P. Carrillo, M. Ángel Medina, A. Díaz-Cuenca, *Acta Biomater.* **2018**, *68*, 272.

[29] T. Distler, A. A. Solisito, D. Schneidereit, O. Friedrich, R. Detsch, A. R. Boccaccini, *Biofabrication* **2020**, *12*, 045005.

[30] J. Hazur, R. Detsch, E. Karakaya, J. Kaschta, J. Teßmar, D. Schneidereit, O. Friedrich, D. W. Schubert, A. R. Boccaccini, *Biofabrication* **2020**, *12*, 045004.

[31] Q. Hu, Y. Li, N. Zhao, C. Ning, X. Chen, *Mater. Lett.* **2014**, *134*, 130.

[32] H. Duan, J. Diao, N. Zhao, Y. Ma, *Mater. Lett.* **2016**, *167*, 201.

[33] M. Etienne, A. Walcarius, *Talanta* **2003**, *59*, 1173.

[34] A. GhavamiNejad, N. Ashammakhi, X. Y. Wu, A. Khademhosseini, *Small* **2020**, *16*, 2002931.

[35] T. Distler, K. McDonald, S. Heid, E. Karakaya, R. Detsch, A. R. Boccaccini, *ACS Biomater. Sci. Eng.* **2020**, *6*, 3899.

[36] T. Kokubo, H. Takadama, *Biomaterials* **2006**, *27*, 2907.

[37] C. Wu, Y. Zhou, M. Xu, P. Han, L. Chen, J. Chang, Y. Xiao, *Biomaterials* **2013**, *34*, 422.

[38] H. Zhu, K. Zheng, A. R. Boccaccini, *Acta Biomater.* **2021**, *129*, 1.

[39] W. Li, P. Nooeaid, J. A. Roether, D. W. Schubert, A. R. Boccaccini, *J. Eur. Ceram. Soc.* **2014**, *34*, 505.

[40] F. Westhauser, S. Decker, Q. Nawaz, F. Rehder, S. Wilkesmann, A. Moghaddam, E. Kunisch, A. R. Boccaccini, *Materials* **2021**, *14*, 1864.

[41] W. Lin, X. Zhu, L. Gao, M. Mao, D. Gao, Z. Huang, *Cell Death Dis.* **2021**, *12*, 147.

[42] Q.-R. Xiao, N. Zhang, X. Wang, X.-Y. Man, K. Yang, L.-X. Lü, N.-P. Huang, *Adv. Mater. Interfaces* **2017**, *4*, 1600652.

[43] L. Ouyang, J. P. K. Armstrong, M. Salmeron-Sanchez, M. M. Stevens, *Adv. Funct. Mater.* **2020**, *30*, 1909009.

[44] C. R. Alcala-Orozco, X. Cui, G. J. Hooper, K. S. Lim, T. B. F. Woodfield, *Acta Biomater.* **2021**, *132*, 188.

[45] X. Cui, J. Li, Y. Hartanto, M. Durham, J. Tang, H. Zhang, G. Hooper, K. Lim, T. Woodfield, *Adv. Healthcare Mater.* **2020**, *9*, 1901648.

[46] W. Xu, B. Z. Molino, F. Cheng, P. J. Molino, Z. Yue, D. Su, X. Wang, S. Willför, C. Xu, G. G. Wallace, *ACS Appl. Mater. Interfaces* **2019**, *11*, 8838.

[47] Q. Gao, X. Niu, L. Shao, L. Zhou, Z. Lin, A. Sun, J. Fu, Z. Chen, J. Hu, Y. Liu, Y. He, *Biofabrication* **2019**, *11*, 035006.

[48] X. Zhai, C. Ruan, Y. Ma, D. Cheng, M. Wu, W. Liu, X. Zhao, H. Pan, W. W. Lu, *Adv. Sci.* **2018**, *5*, 1700550.

[49] A. Schwab, R. Levato, M. D'Este, S. Piluso, D. Eglin, J. Malda, *Chem. Rev.* **2020**, *120*, 11028.

[50] J. M. Lee, W. L. Ng, W. Y. Yeong, *Appl. Phys. Rev.* **2019**, *6*, 011307.

[51] X. Zhao, D. A. Hu, D. Wu, F. He, H. Wang, L. Huang, D. Shi, Q. Liu, N. Ni, M. Pakvasa, *Front. Bioeng. Biotechnol.* **2021**, *9*, 141.

[52] H. Wu, *Ph.D. Thesis*, Multifunctional polymer composites containing inorganic nanoparticles and novel low-cost carbonaceous fillers, Iowa State University **2014**.

[53] W. K. Setiawan, K.-Y. Chiang, *Sustainable Environ. Res.* **2019**, *29*, 32.

[54] N. Wen, T. Song, Z. Ji, D. Jiang, Z. Wu, Y. Wang, Z. Guo, *React. Funct. Polym.* **2021**, *168*, 105041.

[55] A. Phadke, C. Zhang, B. Arman, C.-C. Hsu, R. A. Mashelkar, A. K. Lele, M. J. Tauber, G. Arya, S. Varghese, *Proc. Natl. Acad. Sci. U. S. A.* **2012**, *109*, 4383.

[56] J. Malda, J. Visser, F. P. Melchels, T. Jüngst, W. E. Hennink, W. J. A. Dhert, J. Groll, D. W. Hutmacher, *Adv. Mater.* **2013**, *25*, 5011.

[57] S. Pompili, G. Latella, E. Gaudio, R. Sferra, A. Vetuschi, *Front. Med.* **2021**, *8*, 610189.

[58] C. Bonnans, J. Chou, Z. Werb, *Nat. Rev. Mol. Cell Biol.* **2014**, *15*, 786.

[59] H. Wang, S. C. Heilshorn, *Adv. Mater.* **2015**, *27*, 3717.

[60] B. Yang, K. Wei, C. Loebel, K. Zhang, Q. Feng, R. Li, S. H. D. Wong, X. Xu, C. Lau, X. Chen, *Nat. Commun.* **2021**, *12*, 3514.

[61] X. Zhang, D. Zeng, N. Li, J. Wen, X. Jiang, C. Liu, Y. Li, *Sci. Rep.* **2016**, *6*, 19361.

[62] M. Rizwan, A. E. G. Baker, M. S. Shoichet, *Adv. Healthcare Mater.* **2021**, *10*, 2100234.

[63] J. M. Lee, W. Y. Yeong, *Adv. Healthcare Mater.* **2016**, *5*, 2856.

[64] Y. Ma, N. Hu, J. Liu, X. Zhai, M. Wu, C. Hu, L. Li, Y. Lai, H. Pan, W. W. Lu, X. Zhang, Y. Luo, C. Ruan, *ACS Appl. Mater. Interfaces* **2019**, *11*, 9415.

[65] J.-H. Lee, M.-S. Kang, C. Mahapatra, H.-W. Kim, *PLoS One* **2016**, *11*, e0150727.

[66] L. Zhou, L. Fan, F.-M. Zhang, Y. Jiang, M. Cai, C. Dai, Y.-A. Luo, L.-J. Tu, Z.-N. Zhou, X.-J. Li, C.-Y. Ning, K. Zheng, A. R. Boccaccini, G.-X. Tan, *Bioact. Mater.* **2021**, *6*, 890.

[67] S. N. Rath, P. Nooeaid, A. Arkudas, J. P. Beier, L. A. Strobel, A. Brandl, J. A. Roether, R. E. Horch, A. R. Boccaccini, U. Kneser, *J. Tissue Eng. Regener. Med.* **2016**, *10*, E497.

[68] X. Zhai, C. Ruan, J. Shen, C. Zheng, X. Zhao, H. Pan, W. W. Lu, *J. Mater. Chem. B* **2021**, *9*, 2394.

[69] S. T. Bendtsen, S. P. Quinnell, M. Wei, *J. Biomed. Mater. Res., Part A* **2017**, *105*, 1457.

[70] A. Kosik-Kozioł, M. Costantini, A. Mróz, J. Idaszek, M. Heljak, J. Jaroszewicz, E. Kijeńska, K. Szöke, N. Frerker, A. Barbetta, *Biofabrication* **2019**, *11*, 035016.

[71] L. S. Bertol, R. Schabbach, L. A. L. Dos Santos, *J. Mater. Sci.: Mater. Med.* **2017**, *28*, 168.

[72] S. Romanazzo, T. G. Molley, S. Nemec, K. Lin, R. Sheikh, J. J. Gooding, B. Wan, Q. Li, K. Alan Kilian, I. Roohani, *Adv. Funct. Mater.* **2021**, *31*, 2008216.

[73] Y.-W. Chen, Y.-F. Shen, C.-C. Ho, J. Yu, Y.-H. A. Wu, K. Wang, C.-T. Shih, M.-Y. Shie, *Mater. Sci. Eng., C* **2018**, *91*, 679.

[74] D. Liu, D. C. Genetos, Y. Shao, D. J. Geist, J. Li, H. Zhu Ke, C. H. Turner, R. L. Duncan, *Bone* **2008**, *42*, 644.

[75] S. Zhao, J. Zhang, M. Zhu, Y. Zhang, Z. Liu, Y. Ma, Y. Zhu, C. Zhang, *J. Mater. Chem. B* **2015**, *3*, 1612.

[76] Y. Navaro, N. Bleich-Kimelman, L. Hazanov, I. Mironi-Harpaz, Y. Shachaf, S. Garty, Y. Smith, G. Pelled, D. Gazit, D. Seliktar, Z. Gazit, *Biomaterials* **2015**, *49*, 68.

[77] N. Huebsch, P. R. Arany, A. S. Mao, D. Shvartsman, O. A. Ali, S. A. Bencherif, J. Rivera-Feliciano, D. J. Mooney, *Nat. Mater.* **2010**, *9*, 518.

[78] S. Khetan, M. Guvendiren, W. R. Legant, D. M. Cohen, C. S. Chen, J. A. Burdick, *Nat. Mater.* **2013**, *12*, 458.

[79] R. M. Raftery, I. M. Castaño, G. Chen, B. Cavanagh, B. Quinn, C. M. Curtin, S. Ann Cryan, F. J. O'Brien, *Biomaterials* **2017**, *149*, 116.

[80] S. N. Rath, A. Brandl, D. Hiller, A. Hoppe, U. Gbureck, R. E. Horch, A. R. Boccaccini, U. Kneser, *PLoS One* **2014**, *9*, e113319.

[81] C. Stähli, M. James-Bhasin, A. Hoppe, A. R. Boccaccini, S. N. Nazhat, *Acta Biomater.* **2015**, *19*, 15.

[82] A. R. Boccaccini, U. Kneser, A. Arkudas, *Expert Rev. Med. Devices* **2012**, *9*, 457.

[83] K. C. R. Kolan, J. A. Semon, A. T. Bindbeutel, D. E. Day, M. C. Leu, *Bioprinting* **2020**, *18*, e00075.

[84] Z. Wu, X. Su, Y. Xu, B. Kong, W. Sun, S. Mi, *Sci. Rep.* **2016**, *6*, 24474.

[85] L. Toledo, L. Racine, V. Pérez, J. P. Henríquez, R. Auzely-Velty, B. F. Urbano, *Mater. Sci. Eng., C* **2018**, *92*, 769.

**ADVANCED
SCIENCE NEWS**

www.advancedsciencenews.com

NANO · MICRO

small

www.small-journal.com

[86] C. Zareie, A. R. Bahramian, M. V. Sefti, M. B. Salehi, *J. Mol. Liq.* **2019**, *278*, 512.

[87] Y. Chen, X. Xiong, X. Liu, R. Cui, C. Wang, G. Zhao, W. Zhi, M. Lu, K.e Duan, J. Weng, S. Qu, J. Ge, *J. Mater. Chem. B* **2020**, *8*, 5500.

[88] M. Laurenti, A. A. Subaie, M.-N. Abdallah, A. R. G. Cortes, J. L. Ackerman, H. Vali, K. Basu, Y. L. Zhang, M. Murshed, S. Strandman, *Nano Lett.* **2016**, *16*, 4779.

[89] P. Thoniyot, M. J. Tan, A. A. Karim, D. J. Young, X. J. Loh, *Adv. Sci.* **2015**, *2*, 1400010.

[90] N. Ashammakhi, *J. Craniofacial Surg.* **2005**, *16*, 195.

[91] N. Ashammakhi, E. H. Apu, E. J. Caterson, *J. Craniofacial Surg.* **2021**, *32*, 819.

[92] K. Zheng, J. Kang, B. Rutkowski, M. Gawe¸da, J. Zhang, Y. Wang, N. Founier, M. Sitarz, N. Taccardi, A. R. Boccaccini, *Front. Chem.* **2019**, *7*, 497.

[93] A. El-Fiqi, J. H. Lee, E.-J. Lee, H.-W. Kim, *Acta Biomater.* **2013**, *9*, 9508.

[94] T. Distler, F. Ruther, A. R. Boccaccini, R. Detsch, *Macromol. Biosci.* **2019**, *19*, 1900245.

[95] B. Sarker, D. G. Papageorgiou, R. Silva, T. Zehnder, F. Gul-E-Noor, M. Bertmer, J. Kaschta, K. Chrissafis, R. Detsch, A. R. Boccaccini, *J. Mater. Chem. B* **2014**, *2*, 1470.

[96] C. G. Gomez, M. Rinaudo, M. A. Villar, *Carbohydr. Polym.* **2007**, *67*, 296.

[97] L. Ouyang, R. Yao, Y. Zhao, W. Sun, *Biofabrication* **2016**, *8*, 035020.

2104996 (18 of 18)